

Predicting Frictional Properties of Graphene Kirigami Using Molecular Dynamics and Neural Networks

Designs for a negative friction coefficient.

Mikkel Metzsch Jensen



Thesis submitted for the degree of
Master in Computational Science: Materials Science
60 credits

Department of Physics
Faculty of mathematics and natural sciences

UNIVERSITY OF OSLO

Spring 2023

Predicting Frictional Properties of Graphene Kirigami Using Molecular Dynamics and Neural Networks

Designs for a negative friction coefficient.

Mikkel Metzsch Jensen



© 2023 Mikkel Metzsch Jensen

Predicting Frictional Properties of Graphene Kirigami Using Molecular Dynamics and Neural Networks

<http://www.duo.uio.no/>

Printed: Reprocentralen, University of Oslo

Abstract

Basic introduction

Various numerical models and experimental results propose different governing mechanisms for friction at the nanoscale.

More detailed background

We consider a graphene sheet modified with Kirigami-inspired cuts and under the influence of strain. Prior research has demonstrated that this system exhibits out-of-plane buckling, which could result in a decrease in contact area when sliding on a substrate. According to asperity theory, this decrease in contact area is expected to lead to a reduction in friction.

General problem

However, to the best of our knowledge, no previous studies have investigated the friction behavior of a nanoscale Kirigami graphene sheet under strain.

Summarize main result: “here we show”

Here we show that specific Kirigami designs yield a non-linear dependency between kinetic friction and the strain of the sheet.

General context

Using molecular dynamics simulation, we have found a non-monotonic increase in friction with strain. We found that the friction-strain relationship does not show any clear dependency on contact area which contradicts asperity theory. Our findings suggest that the effect is associated with the out-of-plane buckling of the graphene sheet and we attribute this to a commensurability effect. By mimicking a load-strain coupling through tension, we were able to utilize this effect to demonstrate a negative friction coefficient on the order of -0.3 for loads in the range of a few nN. In addition, we have attempted to use machine learning to capture the relationship between Kirigami designs, load, and strain, with the objective of performing an accelerated search for new designs. While this approach produced some promising results, we conclude that further improvements to the dataset are necessary in order to develop a reliable model.

Broader perspective

We anticipate our findings to be a starting point for further investigations of the underlying mechanism for the frictional behavior of a Kirigami sheet. For instance, the commensurability hypothesis could be examined by varying the sliding angle in simulations. We propose to use an active learning strategy to extend the dataset for the use of machine learning to assist these investigations. If successful, further studies can be done on the method of inverse design. In summary, our findings suggest that the application of nanoscale Kirigami can be promising for developing novel friction-control strategies.

353 words

Various numerical models and experimental results propose different governing mechanisms for friction at the nanoscale. We consider a graphene sheet modified with Kirigami-inspired cuts and under the influence of strain. Prior research has demonstrated that this system exhibits out-of-plane buckling, which could result in a decrease in contact area when sliding on a substrate. According to asperity theory, this decrease in contact area is expected to lead to a reduction in friction. However, to the best of our knowledge, no previous studies have investigated the friction behavior of a nanoscale Kirigami graphene sheet under strain. Here we show that specific Kirigami designs yield a non-linear dependency between kinetic friction and the strain of the sheet. Using molecular dynamics simulation, we have found a non-monotonic increase in friction with strain. We found that the friction-strain relationship does not show any clear dependency on contact area which contradicts asperity theory. Our findings suggest that the effect is associated with the out-of-plane buckling of the graphene sheet and we attribute this to a commensurability effect. By mimicking a load-strain coupling through tension, we were able to utilize this effect to demonstrate a negative friction coefficient on the order of -0.3 for loads in the range of a few nN. In addition, we have attempted to use machine learning to capture the relationship between Kirigami designs, load, and strain, with the objective of performing an accelerated search for new designs. While this approach produced some promising results, we conclude that further improvements to the dataset are necessary in order to develop a reliable model. We anticipate our findings to be a starting point for further investigations of the underlying mechanism for the frictional behavior of a Kirigami sheet. For instance, the commensurability hypothesis could be examined by varying the sliding angle in simulations. We propose to use an active learning strategy to extend the dataset for the use of machine learnig to assist these investigations. If successful, further studies can be done on the method of inverse design. In summary, our findings suggest that the application of nanoscale Kirigami can be promising for developing novel friction-control strategies.

Acknowledgments

Acknowledgments.

List of Symbols

F_N Normal force (normal load)

Acronyms

CM Center of Mass. 11

FFM Friction Force Microscopes. 9

GAN Generative Adversarial Networks. 2, 31

MD Molecular Dynamics. 1, 2, 3, 4, 9, 10, 27, 28, 29

ML Machine Learning. 2, 30

NN Nearest neighbours. 14

SFA Surface force apparatus. 9

Contents

1	Introduction	1
1.1	Motivation	1
1.2	Goals	3
1.3	Contributions	3
1.4	Thesis structure	4
I	Background Theory	5
II	Simulations	7
2	Creating a graphene kirigami system	9
2.1	Region definitions	10
2.2	Numerical procedure	10
2.3	Setting up the substrate	12
2.4	Setting up sheet	13
2.4.1	Indexing	13
2.4.2	Removing atoms	14
2.5	Kirigami patterns	15
2.5.1	Tetrahedron	16
2.5.2	Honeycomb	17
2.5.3	Random walk	17
2.5.3.1	Fundamentals	18
2.5.3.2	Spacing of walking paths	18
2.5.3.3	Bias	19
2.5.3.4	Stay or break	20
2.5.3.5	Deployment schemes	21
2.5.3.6	Validity	22
2.5.3.7	Random walk examples	22
3	Summary	27
3.1	Summary and conclusions	27
3.1.1	Designing an MD simulation	27
3.1.2	Genereting Kirigami patterns	28
3.1.3	Control friction using Kirigami	28
3.1.4	Capturing trends in friction data with machine learning	29
3.1.5	Accelerated search	30
3.1.6	Negative friction coefficient	30
3.2	Outlook	31
Appendices		33
A	Appendix A	35

A Appendix B	37
B Appendix C	39

Chapter 1

Introduction

1.1 Motivation

Friction is the force that prevents the relative motion of objects in contact. From our everyday life, we recognize it as the inherent resistance to sliding motion. Some surfaces appear slippery and some rough, and we know intuitively that sliding down a snow-covered hill is much more exciting than its grassy counterpart. Without friction, it would not be possible to walk across a flat surface, lean against the wall without falling over or secure an object by the use of nails or screws [p. 5] [1]. It is probably safe to say that the concept of friction is integrated into our everyday life to such an extent that most people take it for granted. However, the efforts to control friction date back to the early civilization (3500 B.C.) with the use of the wheel and lubricants to reduce friction in translational motion [2]. Today, friction is considered a part of the wider field *tribology* derived from the Greek word *tribos* meaning “rubbing” and includes the science of friction, wear and lubrication [2]. The most compelling motivation to study tribology is ultimately to gain full control of friction and wear for various technical applications. Especially, reducing friction is of great interest as this has advantages for energy efficiency. It has been reported that tribological problems have a significant potential for economic and environmental improvements [3]:

“On global scale, these savings would amount to 1.4% of the GDP annually and 8.7% of the total energy consumption in the long term.” [4].

On the other hand, the reduction of friction is not the only sensible application for tribological studies. Controlling frictional properties, besides minimization, might be of interest in the development of a grasping robot where finetuned object handling is required. While achieving a certain “constant” friction response is readily obtained through appropriate material choices, we are yet to unlock the full capabilities to alter friction dynamically on the go. One example from nature inspiring us to think along these lines are the gecko feet. More precisely, the Tokay gecko has received a lot of attention in scientific studies aiming to unravel the underlying mechanism of its “toggable” adhesion properties. Although geckos can produce large adhesive forces, they retain the ability to remove their feet from an attachment surface at will [5]. This makes the gecko able to achieve a high adhesion on the feet when climbing a vertical surface while lifting them for the next step remains relatively effortless. For a grasping robot, we might consider an analog frictional concept of a surface material that can change from slippery to rough on demand depending on specific tasks; Slippery and smooth when interacting with people and rough and firmly gripping when moving heavy objects.

In recent years an increasing amount of interest has gone into the studies of the microscopic origin of friction, due to the increased possibilities in surface preparation and the development of nanoscale experimental methods. Nano-friction is also of great concern for the field of nano-machining where the frictional properties between the tool and the workpiece dictate machining characteristics [3]. With concurrent progress in computational capacity and development of Molecular Dynamics (MD), numerical investigations serve as an invaluable tool for getting insight into the nanoscale mechanics associated with friction. This simulation-based approach can be considered as a “numerical experiment” enabling us to create and probe a variety of high-complexity systems which are still out of reach for modern experimental methods.

In materials science such MD-based numerical studies have been used to explore the concept of so-called *metamaterials* where the material compositions are designed meticulously to enhance certain physical properties [6–11]. This is often achieved either by intertwining different material types or removing certain regions completely. In recent papers by Hanakata et al. [6, 7], numerical studies have showcased that the mechanical properties of a graphene sheet, yield stress and yield strain, can be altered through the introduction of so-called *Kirigami* inspired cuts into the sheet. Kirigami is a variation of origami where the paper is cut additionally to being folded. While these methods originate as an art form, aiming to produce various artistic objects, they have proven to be applicable in a wide range of fields such as optics, physics, biology, chemistry and engineering [12]. Various forms of stimuli enable direct 2D to 3D transformations through folding, bending, and twisting of microstructures. While original human designs have contributed to specific scientific applications in the past, the future of this field is highly driven by the question of how to generate new designs optimized for certain physical properties. However, the complexity of such systems and the associated design space makes for seemingly intractable¹ problems ruling out analytic solutions.

Earlier architecture design approaches such as bioinspiration, looking at gecko feet for instance, and Edisonian, based on trial and error, generally rely on prior knowledge and an experienced designer [9]. While the Edisonian approach is certainly more feasible through numerical studies than real-world experiments, the number of combinations in the design space rather quickly becomes too large for a systematic search, even when considering the computation time on modern-day hardware. However, this computational time constraint can be relaxed by the use of machine learning (ML) which has proven successful in the establishment of a mapping from the design space to physical properties of interest. This gives rise to two new styles of design approaches: One, by utilizing the prediction from a trained network we can skip the MD simulations altogether resulting in an *accelerated search* of designs. This can be further improved by guiding the search accordingly to the most promising candidates, for instance, as done with the *genetic algorithm* based on mutation and crossing of the best candidates so far. Another more sophisticated approach is through generative methods such as *Generative Adversarial Networks* (GAN) or diffusion models. The latter is being used in state-of-the-art AI systems such as OpenAI's DALL-E2 [13] or Midjourney [14]. By working with a so-called *encoder-decoder* network structure, one can build a model that reverses the prediction process. This is often referred to as *reverse design*, where the model predicts a design from a set of physical target properties. In the papers by Hanakata et al. [6, 7] both the *accelerated search* and the *inverse design* approach was proven successful to create novel metamaterial Kirigami designs with the graphene sheet.

Hanakata et al. attributes the variation in mechanical properties to the non-linear effects arising from the out-of-plane buckling of the sheet. Since it is generally accepted that the surface roughness is of great importance for frictional properties it can be hypothesized that Kirigami-induced out-of-plane buckling can also be exploited for the design of frictional metamaterials. For certain designs, we might hope to find a relationship between the stretching of the sheet and frictional properties. If significant, this could give rise to an adjustable friction behavior beyond the point of manufacturing. For instance, the grasping robot might apply such a material as artificial skin for which stretching or relaxing of the surface could result in a changeable friction strength.

In addition, the Kirigami graphene properties can be explored through a potential coupling between the stretch and the normal load, through a nanomachine design, with the aim of altering the friction coefficient. This invites the idea of non-linear friction coefficients which might in theory also take on negative values. The latter would constitute a rare property only found a few cases. These are mainly for the unloading phase of adhesive surfaces [15] or the loading phase of particular heterojunction materials [16, 17].

To the best of our knowledge, Kirigami has not yet been implemented to alter the frictional properties of a nanoscale system. However, in a recent paper by Liefferink et al. [18] it is reported that macroscale Kirigami can be used to dynamically control the macroscale roughness of a surface through stretching. They reported that the roughness change led to a changeable frictional coefficient by more than one order of magnitude. This supports the idea that Kirigami designs can be used to alter friction, but we believe that taking this concept to the nanoscale would involve a different set of governing mechanisms and thus contribute to new insight in this field.

¹In computer science we define an *intractable* problem as a problem with no *efficient* algorithm to solve it nor any analytical solutions. The only way to solve such problems is the *brute-force* approach, simply trying all possible solutions, which is often beyond the capabilities of computational resources.

1.2 Goals

In this thesis, we investigate the prospects of altering the frictional properties of a graphene sheet through the application of Kirigami-inspired cuts and stretching of the sheet. With the use of molecular dynamics (MD) simulations, we evaluate the frictional properties of various Kirigami designs under different physical conditions. Based on the MD results, we investigate the possibility to use machine learning for the prediction of frictional properties and subsequently using the model for an accelerated search of new designs. The main goals of the thesis can be summarized as follows.

1. Design an MD simulation procedure to evaluate the frictional properties of a Kirigami graphene sheet under specified physical conditions.
2. Develop a numerical framework to generate various Kirigami designs, both by seeking inspiration from macroscale designs and by the use of a random walk based algorithm.
3. Investigate the frictional behavior under varying load and stretch for different Kirigami designs.
4. Develop and train a machine learning model to predict the MD simulation result and perform an accelerated search of new designs with the scope of optimizing certain frictional properties.

1.3 Contributions

By working towards the goals outlined above (Sec. 1.2), I have discovered a non-linear relationship between the kinetic friction and the strain for certain Kirigami patterns. This phenomenon was found to be associated with the out-of-plane buckling of the Kirigami sheet but with no clear relationship to the contact area or the tension in the sheet. I found that this method does not provide any mechanism for a reduction in friction, in comparison to a non-cut sheet, but the straining of certain Kirigami sheets allows for a non-monotonic increase in friction. The relationship to normal load was proven negligible in this context and I have demonstrated that a coupled system of load and strain (through sheet tension) can exhibit a negative friction coefficient in certain load ranges. Moreover, I have created a dataset of roughly 10,000 data points for assessing the employment of machine learning and accelerated search of Kirigami designs. I have found, that this approach might be useful, but it requires an extended dataset in order to produce reliable results for a search of new designs.

During our investigations, I have built three numerical tools, beyond the regular scripts associated with data analysis, which can be found on Github [19]. The tools are summarized in the following.

- I have written a LAMMPS-based [20] tool for simulating and measuring the frictional properties of a graphene sheet sliding on a substrate. The code is generally made flexible concerning the choice of sheet configuration, system size, simulation parameters and MD potentials, which makes it applicable for further studies within this topic. I have also built an automated procedure to carry out multiple simulations under varying parameters by submitting jobs to a computational cluster via an ssh connection. This was done by adding minor additions to the python package developed by E. M. Nordhagen [21].
- I have generated a Python-based tool for generating Kirigami patterns and exporting these in a compatible format with the simulation software. The generation of molecular structures is done with the use of ASE [22]. Our software includes two classes of patterns inspired by macroscale designs and a random walk algorithm which allow for a variety of different designs through user-defined biases and constraints. Given our system size of choice, the first two pattern generators are capable of generating on the order of 10^8 unique designs while the random walk generator allows for significantly more.
- I have built a machine learning tool based on Pytorch [23] which includes setting up the data loaders, a convolutional network architecture, a loss function, and general algorithms for training and validating the results. Additionally, I have written several scripts for performing grid searches and analyzing the model predictions in the context of the frictional properties of graphene.

All numerical implementations used for this thesis have been originally developed for the purpose with the exception of the usage of libraries as mentioned above and commonly known Python libraries such as Numpy and Matplotlib.

1.4 Thesis structure

The thesis is divided into two parts. In Part I we introduce the relevant theoretical background, and in Part II we present the numerical implementations and the results of this thesis.

Part I contains a description of the theoretical background related to Friction (??), Molecular Dynamics (??) and Machine Learning (??). In ?? we will formulate our research questions in the light of the friction theory.

In Part II, we begin by presenting our definition and setting up of the system in Chapter 2. This includes the MD simulations and the generation of Kirigami designs. This is followed by a pilot study in ?? where we evaluate the simulation results for various physical conditions and compare a non-cut sheet to two different Kirigami designs. Further explorations of the Kirigami configurations are carried out in ?? which includes the generation of a dataset and the employment of machine learning and an accelerated search. We use the results from the pilot study to demonstrate the possibility to achieve a negative friction coefficient for a system with coupled load and strain in ?. Finally, we summarize our results and provide an outlook for further studies in Chapter 3. Additional figures are shown in ??, ?? and ??.

Part I

Background Theory

Part II

Simulations

Chapter 2

Creating a graphene kirigami system

The system definition plays an essential role in the “friction experiment” that we are going to carry out through MD simulations. The purpose of the simulations is to quantify the friction that arises when a stretched Kirigami graphene sheet slides over a substrate. We aim to design the simplest possible system that allows for such a measurement under variations of Kirigami design, strain and load.

For this purpose, two approaches were considered as sketched in Fig. 2.1. One approach is simply to mimic a FFM type experiment where the graphene sheet is resting on a substrate and a moving body scans across the graphene surface as seen in Fig. 2.1b. This setup allows for a variety of tip designs, and we can even substitute the tip for a flat surface making the setup resemble a SFA experiment instead. For this setup, we would attach a pre-stretched sheet to the substrate and require the edges of the sheet to be fixated on the substrate to sustain the stretch. Thus, the sheet and substrate would constitute the manufactured object and the moving body would represent the contact to the outside world. In this approach, the potential applications would relate to certain effects being associated with a constant strain value. Another approach is to have the sheet ends fixated on the moving body instead as shown in Fig. 2.1a. This switches the roles of the involved parts as we now view the moving body and the sheet as the manufactured object while contact with the substrate represents the outside world. This allows for the introduction of a nanomachine design that converts the load to a strain of the sheet. Thus, the possible applications allow for a dynamic effect with changing strain through the loading of the sheet. While both methods serve as novel approaches with prospects of providing valuable insight into a sparsely covered field, we choose the latter option (Fig. 2.1a) due to the increased application possibilities.

We do not attempt to model the nanomachine explicitly, but we will use the conceptual idea of a coupling between load and strain to motivate our study. Hence our system of choice consists of a 2D graphene sheet with locked ends, mimicking the attachment to a moving body, and a 3D silicon bulk substrate.

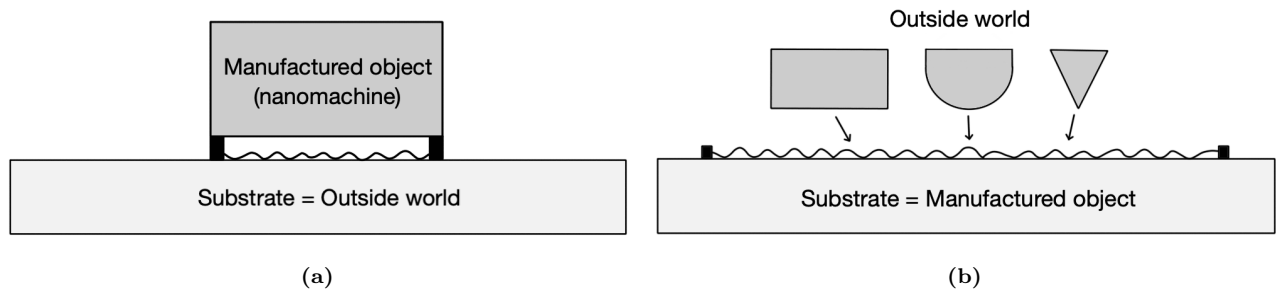


Figure 2.1: Conceptual visualization of two different system setups considered. The wiggly line represents the Kirigami sheet. (a) The chosen setup with a manufactured object connected to the sheet. The contact with the substrate represents the contact with the outside world. (b) An alternative setup where the sheet is fixed in the substrate constituting the manufactured object. The contact with the outside world is then represented through an indentation by objects with various shapes and sizes.

2.1 Region definitions

We subdivide the two main parts of the system, the sheet and the substrate, into specific regions according to their functionality in the MD simulations. For the sheet, we denote a subsection of the ends, with respect to the sliding direction, as so-called *pull blocks*, which is reserved for the application of normal load, stretching, dragging of the sheet, and for applying the thermostat. The remaining *inner sheet* is left for the Kirigami cuts and is simulated as an *NVE* ensemble. This partitioning is motivated by the idea that we want to minimize direct manipulations on the inner sheet, given its presumed critical role in governing friction behavior. The pull blocks are equally split between a thermostat part and a rigid part. It should be noted that the rigidness of the pull blocks is enforced only after a relaxation period to ensure that the crystal structure is fully relaxed. This is further explained in Sec. 2.2. The substrate is equally divided into three parts: The *upper layers* (*NVE*) responsible for the sheet-substrate interaction, the *middle layers* being a thermostat (*NVT*), and the *bottom layers* being frozen, made rigid and fixed, in the initial lattice structure to ensure that the substrate stays in place. Fig. 2.2 show the system is displayed with colors matching the three distinct roles:

1. Red: *NVE* parts which are governing the frictional behavior of interest.
2. Green: Thermostats (*NVT*) surrounding the *NVE* parts in order to modify the temperature without making disturbing changes to the interaction of the sheet and substrate.
3. Blue: Parts that are initially or eventually turned into rigid objects. For the substrate, this refers to an additional fixation as well.

The full sheet is given a size $\sim 130 \times 163 \text{ \AA}$ while the substrate is scaled accordingly to the sheet which is further specified in Sec. 2.3. For an expected strain of 200% the total system size is roughly 55×10^3 atoms. The specific distribution of atoms is shown in Table 2.2 along with the spatial x-y-measures in Table 2.1. An example of a strained sheet is shown in Fig. 2.3

Table 2.1: Specification of the spatial size of the system for the x-y-dimensions with a substrate scaled for an expected sheet strain of 200%. The first column denotes the size relative to the full sheet size $x_S \times y_S$, while the second column denotes the corresponding length in \AA .

Region	Dim	Dim [\AA]	Area [nm^2]
Full sheet	$x_S \times y_S$	$130.029 \times 163.219 \text{ \AA}$	212.23
Inner sheet	$x_S \times 0.81 y_S$	$130.029 \times 132.853 \text{ \AA}$	172.74
Pull blocks	$2 \times x_S \times 0.09 y_S$	$2 \times 130.029 \times 15.183 \text{ \AA}$	2×19.74
Substrate	$1.16 x_S \times 3.12 y_S$	$150.709 \times 509.152 \text{ \AA}$	767.34

Table 2.2: Specification of the system size regarding the number of atoms for various system regions. These numbers correspond with the case of no cuts applied to the sheet and a substrate scaled for the expected stretch of 200%.

Region	Total	Sub region	Sub total	NVE	NVT	Rigid
Full sheet	7800	Inner sheet	6360	6360	0	0
		Pull blocks	1440	0	720	720
Substrate	47376	Upper	15792	15792	0	0
		Middle	15792	0	15792	0
		Bottom	15792	0	0	15792
All	55176			22152	16512	16512

2.2 Numerical procedure

Following the system setup as described previously, the next step involves letting the system relax and reach a stable equilibrium. During this phase, slight modifications to the sheet-substrate distance and lattice spacing

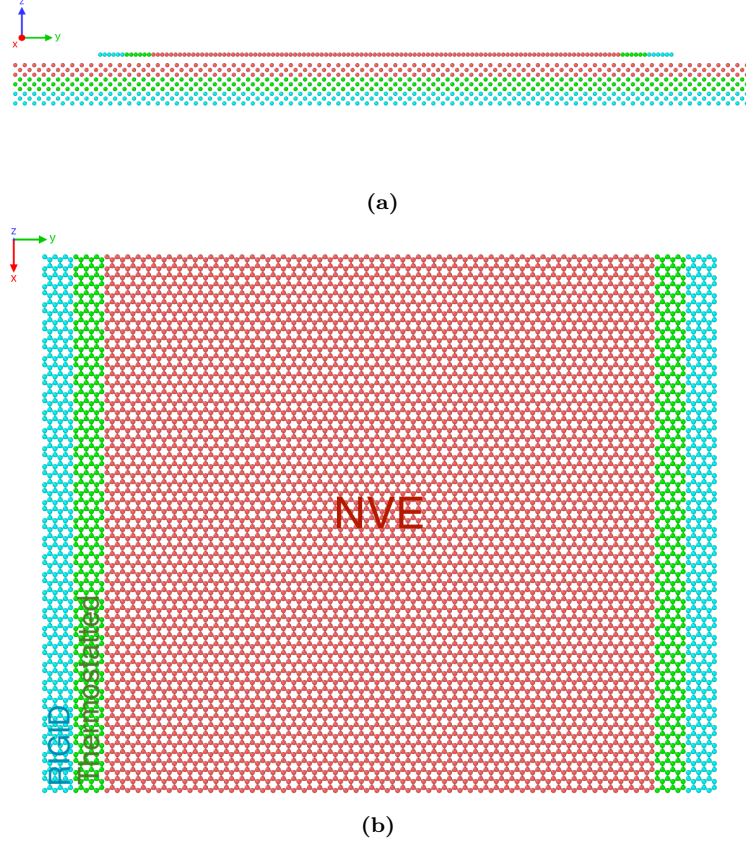


Figure 2.2: System configuration colorized to indicate NVE parts (red), thermostat parts (green) and rigid parts (blue). (a) Side view showing the sheet on top of the substrate. (b) Top view showing only the sheet

take place, both of which are influenced by the thermostat's target temperature. We then stretch the sheet to the desired length, apply normal load and finally slide it along the substrate. The full numerical procedure can be arranged into the following steps. Some steps have been given a default duration denoted in parentheses in units of ps, 10^{-12} seconds.

1. **Relaxation** (15 ps): The sheet and substrate are relaxed for 15 ps after being added in their crystalline form with a separation distance of 3 Å. Given that the equilibrium separation distance will vary with temperature, this value is based on an average estimate suiting our temperature range of interest. In order to avoid any sheet drift we constrain it with the use of three hard spring forces with a spring constant $10^5 \text{ eV}/\text{\AA}^2 \sim 1.6 \times 10^6 \text{ N/m}$: One spring attaches the sheet center of mass (CM) to its original position, preventing CM drift, while the remaining two springs are attached to the pull blocks CM, to prevent rotation. In principle, fixing only one of the pull blocks would suffice, but we choose to fixate both to maintain symmetry. During the relaxation phase, we consider the pull blocks to be rigid with respect to the z-direction only (perpendicular to the sheet). That is, all the forces in the z-direction are summed up and applied as a uniform external force, while the pull blocks are free to expand and contract in the x-y-plane. This feature is incorporated to allow the sheet pull blocks to readjust the lattice spacing according to the temperature of the system. For the following steps, the pull blocks are made truly rigid with respect to all directions, and the spring forces are terminated.
2. **Stretch**: To stretch the sheet, the two opposing rigid parts of the pull blocks are moved apart at a constant velocity until the desired strain level is achieved. The duration of this phase is determined by the values of the *stretch speed* and *stretch amount* parameters.
3. **Pause** (5 ps): The sheet is relaxed for 5 ps to ensure that the sheet is stable and equilibrated after the applied strain deformation.

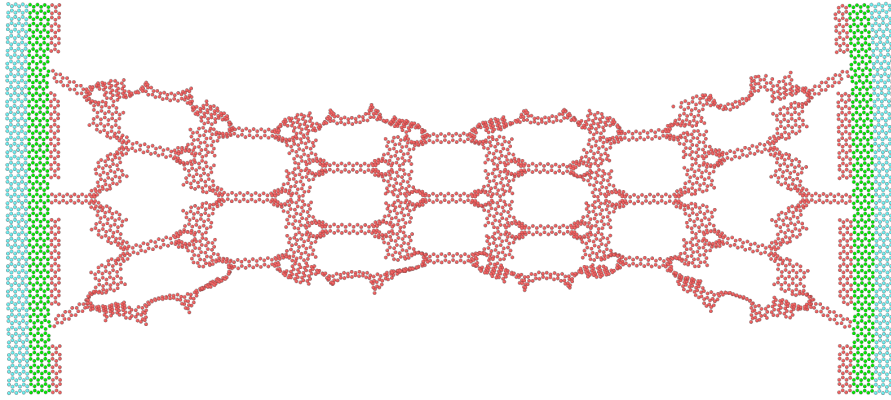


Figure 2.3: Stretched Kirigami sheet against a substrate. The substrate is excluded from the image for better visibility. The atoms are colorized to indicate NVE parts (red), thermostat parts (green) and rigid parts (blue). The pattern used is the Honeycomb (2, 2, 1, 5) (see Chapter 2) at a 100% strain level.

4. **Normal load** (5 ps): The pull blocks are subjected to a uniformly applied load in the negative z-direction, thereby pushing the sheet perpendicularly into the substrate. Initially a viscous damping force, $F = -\gamma \mathbf{v}$ with damping factor γ and velocity v , is added to resist rapid acceleration of the sheet and prevent a hard impact between the sheet and substrate. The damping coefficient is set to $\gamma = 8 \times 10^{-4} \text{ nN}/(\text{m/s})$ and terminated after 0.5 ps which was found to be suitable for the extreme load cases of our intended range. The remaining 4.5 ps is devoted to further relaxation in order to reach a sheet-substrate distance equilibrium.
5. **Sliding:** A virtual atom is introduced into the simulation which exclusively interacts with the rigid parts of the pull blocks through a spring force with spring constant K in the x-y-plane. The force in the z-direction is not influenced by the spring force and is instead governed by the equilibrium between the normal load and the normal response from the sheet-substrate interaction. The virtual atom is immediately given a constant velocity, given by the *sliding speed* parameter. This results in an initial linear increase in sliding force proportional to sliding speed and spring constant $F_{slide} \propto K v_{slide} t$. An infinite spring constant can also be enforced for which the spring is omitted and the pull blocks are moved rigidly with a constant speed.

To limit the complexity of the friction behavior we want to consider systems without wear. To make sure that no wear is taking place for the sheet, we monitor the nearest neighbors for each atom throughout the simulation. At the initial timestep the three nearest neighbors, sitting at a distance 1.42 \AA , of all graphene atoms are recorded. If any of these nearest neighbors exceeds a threshold distance of 4 \AA , indicating a bond breakage, this is marked as a rupture and we halt the simulation. By conducting several test simulations involving high loads and sliding speeds, we have visually confirmed that no wear occurs in the substrate, which demonstrates significantly greater wear resistance than the sheet. Therefore, we do not need to monitor the substrate for any signs of wear.

2.3 Setting up the substrate

The substrate is created as a rectangular slab of Silicon (Si). We create the initial configuration according to its crystalline structure given as a diamond cubic crystal with a lattice parameter $a_{\text{Si}} = 5.43 \text{ \AA}$. The default substrate thickness is chosen such that 9 layers of atoms appear (2 unit cells) corresponding to a thickness of 10.86 \AA . The x-y dimensions are chosen to match the dimensions of the sheet. That is, we define a margin between the sheet edge and the substrate edge for the x- and y-direction respectively. Since we use periodic boundary conditions a too small margin would result in the sheet edges interacting with themselves through the boundary. The absolute lower limit for the margin choice is half the cut-off distance for the Tersoff potential, governing the graphene sheet interaction, at $R + D = 2.1 \text{ \AA}$. However, due to fluctuations in the sheet, we cannot set the margin too close to that limit. In addition, we need to consider the buckling of the sheet as it is stretched, which might cause an expansion in the x-direction for certain configurations. We choose an x-margin

of 20 \AA which provides $2 \cdot 20\text{ \AA} - 2.1\text{ \AA} = 37.9\text{ \AA}$ of additional spacing with respect to the absolute lower limit. By looking over the simulation result visually we confirm that this leaves more than enough room in the cases of extreme buckling. For the y -direction the rigid parts of the pull-blocks moves a certain distance based on the strain value exclusively, and we define the y -margin based on the remaining distance to the edge after stretching. However, as the sheet travels through the periodic boundaries in the y -direction when sliding, we want to add some additional spacing through the y -margin in order to let the substrate surface relax before interacting with the sheet a second time. We choose a y -margin of 15 \AA for which the preferred sliding speed of $20\text{ m/s} = 2\text{ \AA/ps}$ gives 15 ps of relaxation time between encounters with the sheet, similar to the initial relaxation time.

2.4 Setting up sheet

The sheet consists of graphene, which is a single layer of carbon atoms arranged in a hexagonal lattice structure. The bulk version of graphene is graphite and is a stacked structure of multiple graphene layers. We can describe the graphene 2D crystal structure in terms of its primitive lattice vectors \mathbf{a}_1 and \mathbf{a}_2 and a basis. The basis describes the atoms associated with each lattice site, and we populate the lattice by translating the basis by any linear combination of the lattice vectors

$$\mathbf{T}_{mn} = m\mathbf{a}_1 + n\mathbf{a}_2, \quad m, n \in \mathbb{N}.$$

For graphene, we have the primitive lattice vectors [24]

$$\mathbf{a}_1 = a \left(\frac{\sqrt{3}}{2}, -\frac{1}{2} \right), \quad \mathbf{a}_2 = a \left(\frac{\sqrt{3}}{2}, \frac{1}{2} \right), \quad |\mathbf{a}_1| = |\mathbf{a}_2| = a = 2.46\text{ \AA}. \quad (2.1)$$

Notice that we deliberately excluded the third coordinate as we only consider a single graphene layer and thus we do not have to consider the stacking structure of 3D graphite. The basis consists of two carbon atoms given as

$$\left\{ \left(0, 0 \right), \frac{a}{2} \left(\frac{1}{\sqrt{3}}, 1 \right) \right\}. \quad (2.2)$$

The crystal structure is visualized in Fig. 2.4. The hexagonal lattice structure makes for an equal spacing all pairs of atoms with an interatomic distance

$$\left\| \frac{a}{2} \left(\frac{1}{\sqrt{3}}, 1 \right) \right\| \approx 1.42\text{ \AA}.$$

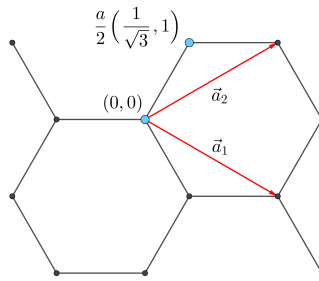


Figure 2.4: Illustration of the graphene crystal structure. The dots represent atom sites, blue dots denote the basis atoms (Eq. (2.2)) and the red arrows denote the primitive lattice vectors (Eq. (2.1)).

2.4.1 Indexing

In order to describe the Kirigami cut patterns applied to the graphene sheet we require an indexing system that provides a unique representation of the atoms in the lattice. This allows us to represent the pattern as a

binary matrix, where 0 denotes removed atoms and 1 denotes present atoms. We let the x-coordinate correspond with the so-called *armchair* direction of the sheet and the y-coordinate with the so-called *zigzag* direction. Notice that the x-coordinate will point to *zigzag* chains of atoms for which the starting point $(x, 0)$ is not evenly spaced as illustrated in Fig. 2.5. Other solutions might naturally involve the lattice vectors, but since these are used to translate between similar basis atoms it introduces an unfortunate duality as one would then need to include the basis atom of choice into the indexing system as well. Additionally, we want an indexing system that conserves the relative physical position of neighbors. That is, atom (i, j) should be in the proximity of $\{(i+1, j), (i-1, j), (i, j+1), (i, j-1)\}$. However, due to the hexagonal structure of the lattice, only three said neighbor indexes will be actual nearest neighbors in the lattice. While $(i, j \pm 1)$ is always the nearest neighbor, the index of the nearest neighbor in the x-direction oscillates for each incrementing of the x- or y-coordinate. That is, the nearest neighbors NN are decided as

$$\begin{aligned} (i+j) \text{ is even} &\rightarrow \text{NN} = \{(i-1, j), (i, j+1), (i, j-1)\}, \\ (i+j) \text{ is odd} &\rightarrow \text{NN} = \{(i+1, j), (i, j+1), (i, j-1)\}. \end{aligned} \quad (2.3)$$

We can visually verify this by consulting Fig. 2.5, which shows that the nearest neighbor indexes depend on whether the atom is oriented to the right or left side in the zigzag chain.

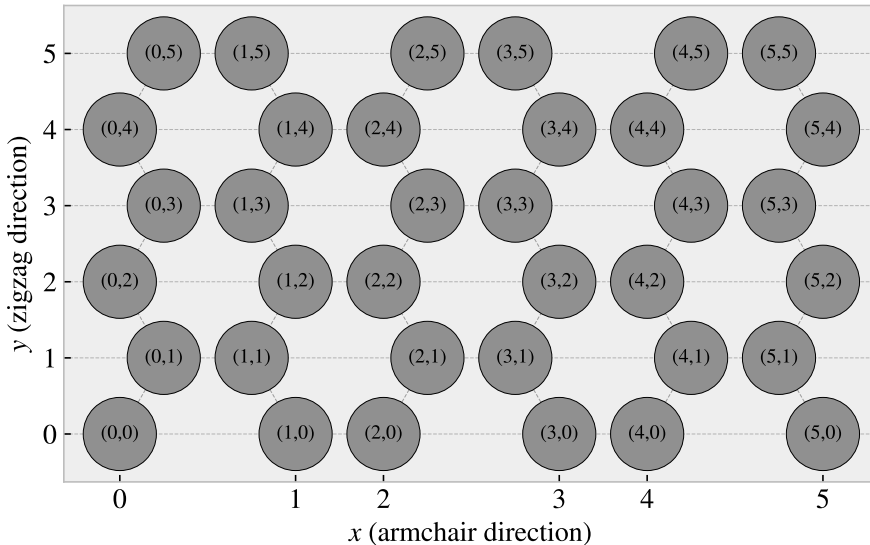


Figure 2.5: Illustration of the graphene atom site indexing. The x-coordinate increment along the armchair direction (pointing to zigzag chains) while the y-coordinate increment along the zigzag direction.

2.4.2 Removing atoms

To simplify the formulation of the cut patterns, we introduce the *center element* which is placed in each gap of the hexagonal honeycomb structure. This is shown in figure Fig. 2.6. These are not populated by any atoms but will serve as a reference for the algorithmic approaches of defining a cut pattern.

The nearest neighbors of the center element alternate with position, similar to the atom site indexing. However, this time it is only dependent on the x-coordinate position. Each center element has six nearest neighbors, in a clockwise direction we can denote them: “up”, “upper right”, “lower right”, “down”, “lower left”, “upper left”. The “up” and “down” neighbors are always accessible as $(i, j \pm 1)$. However, for even i the $(i+1, j)$ index corresponds to the “lower right” neighbour while for odd i this corresponds to the “upper right” neighbour. This shifting applies for all left- or right-oriented neighbors and the full neighbor list is illustrated in Fig. 2.7.

We define a cut pattern by connecting center elements in connected paths. As we walk from center element to center element we remove atoms according to one of two rules

1. Remove intersecting atoms: We remove the pair of atoms placed directly in the path we are walking. That is, when jumping to the “up” center element we remove the two upper atoms located in the local hexagon of atoms. This method is sensitive to the order of the center elements in the path.

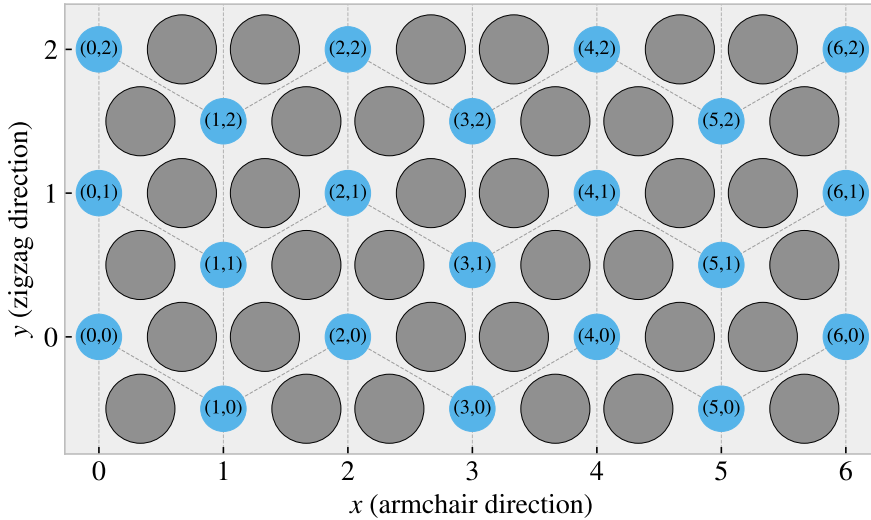


Figure 2.6: Illustration of the indexing for the introduced center element. The y-coordinate increment along the zigzag direction (pointing to armchair chains) while the x-coordinate increment along the armchair direction.

2. Remove all surrounding atoms: We simply remove all atoms in the local hexagon surrounding each center element. This method is independent of the ordering of center elements in the path.

We notice that removing atoms using either of these rules will not guarantee an injective, one-to-one, mapping. The first rule, being path dependent, will more often result in a unique result. However, for both methods, it is possible to construct two different paths leading to the same cut pattern as shown in the following example:

$$\begin{aligned}
 \text{Path 1: } & (i, j) \rightarrow \underbrace{(i+1, j+1)}_{\text{upper right}} \rightarrow \underbrace{(i, j+1)}_{\text{up}} \rightarrow \underbrace{(i+1, j+2)}_{\text{upper right + up}} \rightarrow \underbrace{(i+1, j+1)}_{\text{upper right}} \\
 \text{Path 2: } & (i, j) \rightarrow \underbrace{(i+1, j+1)}_{\text{upper right}} \rightarrow \underbrace{(i+1, j+2)}_{\text{upper right + up}} \rightarrow \underbrace{(i, j+1)}_{\text{up}}
 \end{aligned}$$

Illustrate the example path, because I think it is otherwise impossible to follow.

For the second rule, it is even more obvious that different paths can result in the same final pattern. For instance, if we incircle a center element completely there will be no surrounding atoms left to remove when jumping to that center element. This highlights the motivation for defining the atom-based indexing system which yields an injective mapping between the binary matrix and the graphene lattice. However, using the center elements as a reference makes it easier to design the cut patterns since we can always go in one of the six directions defined by the center element neighbors. In contrast, the atom indexing system has alternating directions for its neighbors, making it more complicated to define cut patterns.

2.5 Kirigami patterns

We propose a series of Kirigami-inspired cut patterns for the altering of the graphene sheet. We seek inspiration from macroscale patterns that showcases a considerable amount of out-of-plane buckling when stretched. We choose to imitate two different designs: 1) An alternating repeating series of perpendicular cuts as shown in Fig. 2.8a popularly used in studies of morphable metematerials [25]. This pattern produces surface buckling with a tetrahedron (three-sided pyramid) shape when stretched. 2) A more intricate pattern shown in Fig. 2.8b which is used commercially by ScotchTM Cushion LockTM [26] as protective wrap for items during shipping. This pattern buckles into a hexagonal honeycomb structure when stretched. In addition to the modeling of the so-called *Tetrahedron* and *Honeycomb* patterns, we also create a series of random walk patterns.

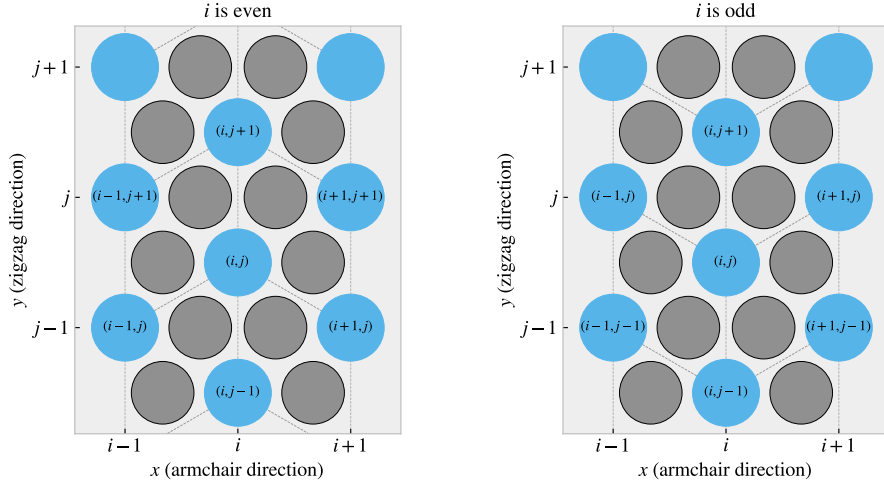


Figure 2.7: Illustration of the center element neighbor indexes for the case when the x-coordinate i is even (left) and i is odd (right).

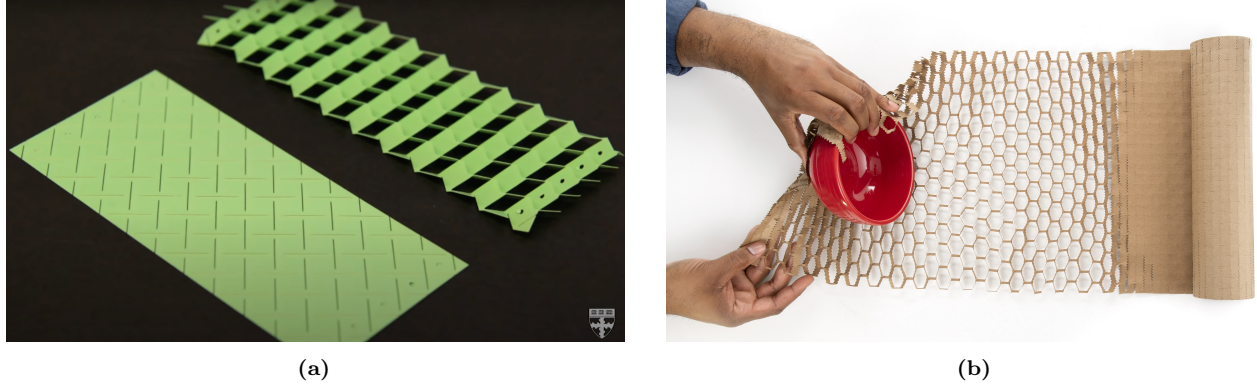


Figure 2.8: Macroscale kirigami cut patterns used as inspiration for the nanoscale implementation. (a) Tetrahedron: Alternating perpendicular cuts producing a tetrahedron shaped surface buckling when stretched. Reprinted from [25]. (b) Honeycomb: Scotch™ Cushion Lock™ [26] producing a honeycomb-shaped surface buckling when stretched.

2.5.1 Tetrahedron

The *Tetrahedron* pattern is defined in terms of center elements for which all atoms surrounding a given center element are removed. The pattern consists of two straight cuts, referred to as line 1 and line 2, that are arranged perpendicular to each other. The lines are positioned such that the center of one line aligns with the other line, and with a given spacing in between. This is illustrated in Fig. 2.9. In order to achieve perpendicular cuts we cannot rely purely on the six center element directions corresponding to the center element neighbors which are spaced by 60° . We let line 1 run along the center elements in the direction of the “upper right” (and “lower left”) center elements, while line 2 goes in the direction between the “down” and “lower right” (“up” and “upper left”) center elements, corresponding to the direction $(1/\sqrt{3}, -1)$. We define variations of the pattern by the number of center elements L_1 and L_2 in line 1 and 2 respectively, together with the spacing between the lines d , as the tuple (L_1, L_2, d) . The pattern is constructed by translating the two lines to the whole sheet according to the spacing. Due to the alignment criteria of having one line point to the center of the other line, we can only allow an odd line length. Furthermore, in order to ensure that each center element is translated to an i -index of similar odd or evenness, we must in practice require that $|L_2 - L_1| = 2, 6, 10, \dots$. Fig. 2.9 shows a visual representation of the pattern components for the $(7, 5, 2)$ pattern.

In addition to the three parameters L_1, L_2, d , the pattern is also anchored to a reference point that describes the position of line 1 and line 2 before being translated to span the sheet. Due to the repeating structure of

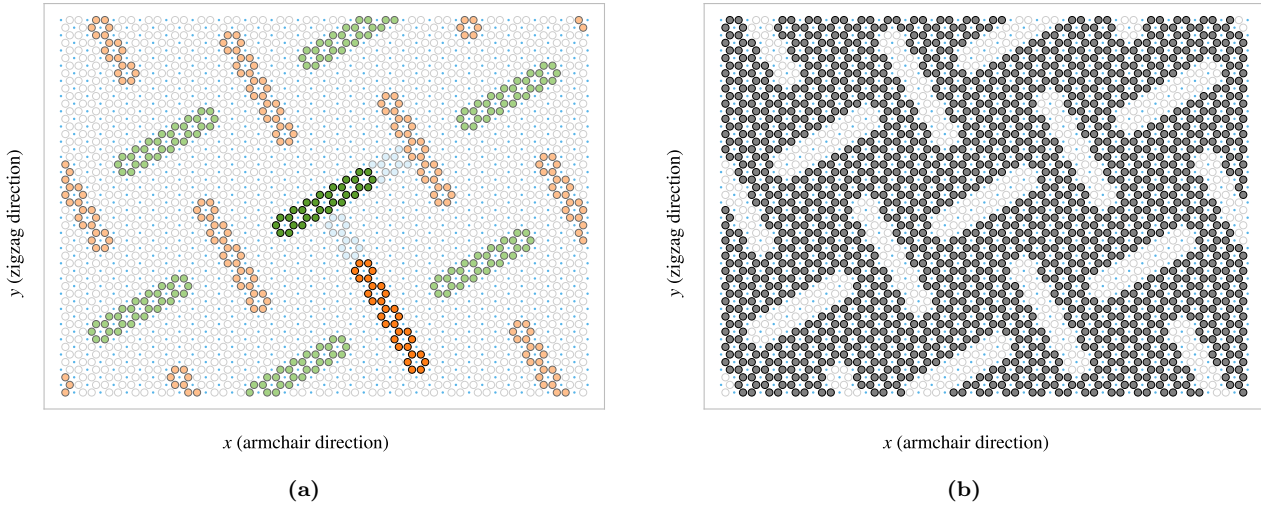


Figure 2.9: Visual representation of the Tetrahedron pattern consisting of two perpendicular lines, line 1 and line 2, of length L_1 and L_2 respectively, with spacing d . This example uses $(L_1, L_2, d) = (7, 5, 2)$ and a sheet matrix size 40×50 corresponding to 2000 atom sites and an approximate sheet size of $84 \times 77 \text{ \AA}$. The non-filled circles represent the possible atom site positions and the blue dots are the center elements. (a) Highlights the removed atoms in the pattern. Line 1 is shown in green and line 2 in orange, with lighter colors for the translated variations. The spacing is indicated in light blue. (b) The sheet after applying the cut pattern with grey circles denoting present atoms.

the pattern, there exist a small finite number of unique reference positions. For the pattern $(7, 5, 2)$ used as an example in Fig. 2.9, there are 140² unique reference points. Some additional variation of the pattern is showcased in Fig. 2.10 each with a reference position at the center of the sheet. Note that a smaller sheet size is used in both Fig. 2.9 and Fig. 2.10 for illustrative purposes.

2.5.2 Honeycomb

The *Honeycomb* pattern is defined, similarly to the Tetrahedron pattern, in terms of the center elements for which all surrounding atoms are removed. The Honeycomb pattern is built from a repeating series of cuts reminiscent of the Roman numeral one rotated by 90° (I^\perp). For a given spacing these are put next to each other in the x-direction, $\text{I}^\perp \text{I}^\perp \text{I}^\perp$, to achieve a row where only a thin *bridge* in between is left to connect the sheet vertically in the y-direction. By placing multiple rows along the y-direction with alternating x-offset we get the class of honeycomb patterns as visualized in Fig. 2.11. The pattern is described in terms of the parameters: (x-width, y-width, bridge thickness, bridge length) which is annotated in Fig. 2.11a with the parameters $(2, 2, 1, 5)$ used as an example. Some additional variations of the pattern class are showcased in Fig. 2.12.

2.5.3 Random walk

The random walk serves as a method for generating Kirigami patterns with randomized features. The motivation for doing this is to create an ensemble of patterns that populate the configuration space more broadly than the more systematic patterns described earlier. This is thought to be important for the quality of the dataset used for machine learning. By this argument, a straightforward way to create random configurations could be achieved simply by random noise, either uniform or Gaussian. However, this would often leave the sheet detached with lots of non-connected atom clusters. Intuitively, we do not find this promising for the generation of large-scale structures which we hypothesize to be of interest. The random walk pattern generation is characterized by the parameters summarized in Table 2.3 which will be introduced throughout the following paragraphs.

²The general formula for calculating this number is rather complicated in comparison to its importance in this context. Therefore, we have omitted the formula and only provide the numerically backed result for the specific parameter set. The derivation of the formula was also deemed not to be rigorous enough.

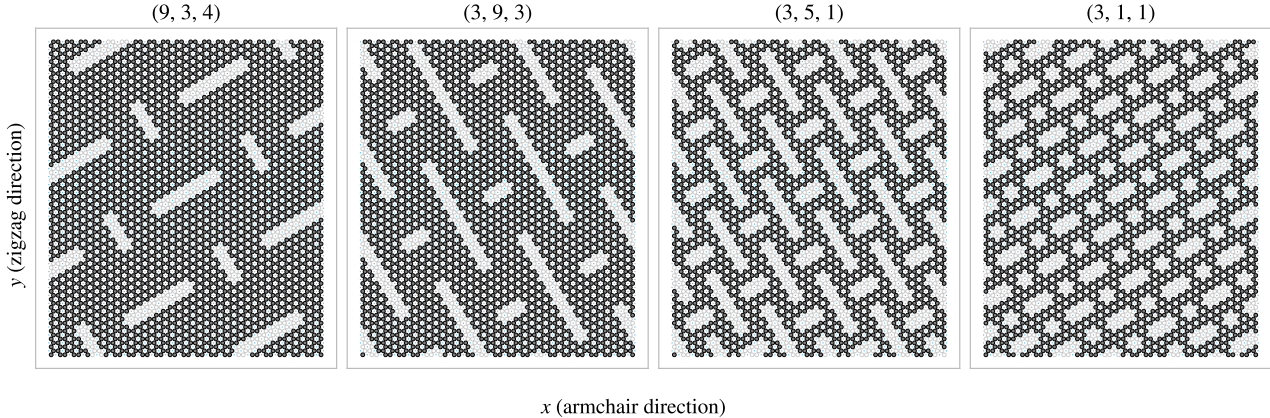


Figure 2.10: Example of different Tetrahedron cut pattern variations. The specific parameters are noted as titles and all of the patterns use the center of the sheet as a reference position. The circles in the figure represent atom sites, where grey-filled circles indicate the presence of atoms and transparent circles indicate removed atoms. The blue dots in the figure indicate the center elements. The sheet matrix size is 40×80 corresponding to 3200 atom sites and an approximate sheet size of $84 \times 123 \text{ \AA}$.

2.5.3.1 Fundamentals

For an uncut sheet, we deploy M random walkers, one at a time, and let them walk for a maximum number of S steps. We can either let the walker travel between atom sites, removing the atoms in the path as it goes, or between the center elements, removing all surrounding atoms. This is managed by setting the *connection* parameter to either *atom* or *center elements*. The method of removing only the intersecting atoms between center elements was also incorporated, but we ended up not using it due to plenty of other interesting options. Nonetheless, we will always remove a site once visited such that the walker itself, or any other walkers, cannot use this site again. This leads to a self-avoiding random walk, meaning that the walker does not cross its own path. However, it furthermore constrains the walkers to avoid the path taken by any previous walker, and thus we might denote this property as “other avoiding”. By default, the walker has an equal chance of choosing any of its adjacent neighbors for the next step, i.e. we draw the next step from a discrete uniform distribution. Optionally we can use periodic boundary conditions, by setting the parameter *periodic* to true or false, allowing neighboring sites to be connected through the edge in both the x and y-direction. When traveling on atom sites this ensures that we have three neighbor options for the next step while traveling on the center elements this gives six neighbor options. If the walker happens to arrive at an already visited site the walk is terminated early. Optionally, we can choose to remove any neighboring sites already visited from the neighbor list and choose uniformly between the remaining options instead. This is done by setting the parameter *avoid invalid* to true. This prolongs the walking distance, but the walker is still able to find itself in a situation where no neighboring sites are available. Note that the walker is not allowed to backtrack its own path either, and thus in such a case the walk will be terminated despite the setting of *avoid invalid*.

2.5.3.2 Spacing of walking paths

To control the spacing between the paths of the various walkers, we implement a so-called *minimum distance* parameter, taking integer values ≥ 0 . This parameter describes the minimum spacing required between paths in terms of the least amount of walking steps. When a walker has ended its walk, either by early termination or hitting the maximum limits of steps, all sites within walking distance of the minimum distance are marked as visited, although they are not removed from the sheet. This prevents any subsequent walkers to visit those sites in their walk according to the general behavior introduced in the previous paragraph. In practice, this is done through a recursive algorithm as described in Algorithm 1. For a given path the function *walk_distance()* is called with the input being a list of all sites in the given paths. The function gathers all the neighbors of each site, regardless of their state on the sheet. It then calls itself recursively using this neighbor list as input, while incrementing a distance counter that is also passed along as an argument. This results in an expansion along all possible outgoing paths from the initial path of interest. Once the distance limit is reached, the function returns

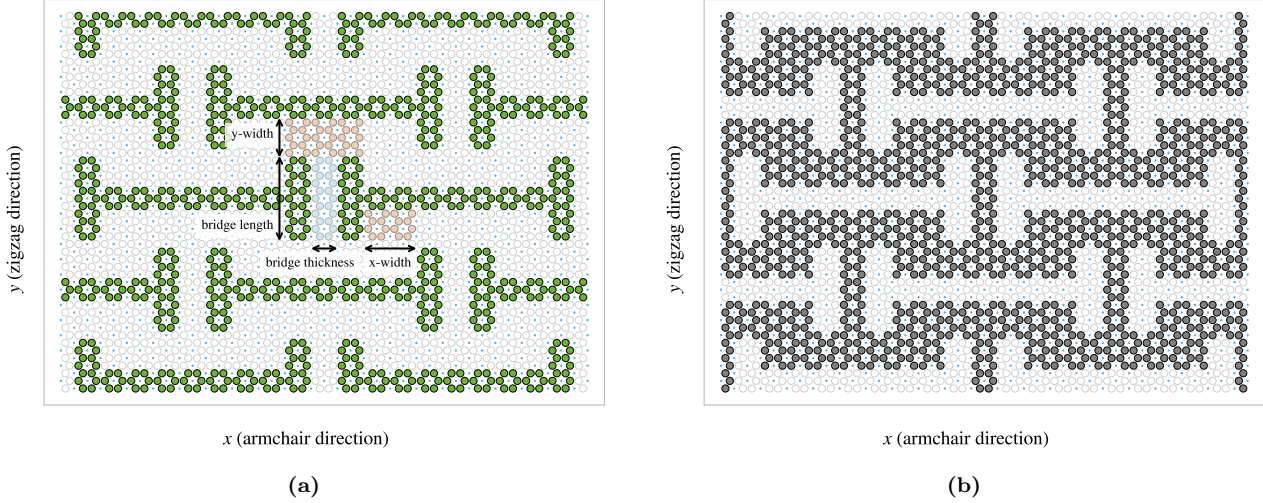


Figure 2.11: Visual representation of the Honeycomb pattern defined by the (x-width, y-width, bridge thickness, bridge length) parameters as annotated on the figure. This example uses the parameters (2, 2, 1, 5) and a sheet matrix size 40×50 corresponding to 2000 atom sites and an approximate sheet size of $84 \times 77 \text{ \AA}$. The non-filled circles represent the possible atom site positions and the blue dots are the center elements. (a) Highlights the removed atoms in the pattern with annotations for the four defining parameters. (b) The sheet after applying the cut pattern with grey circles denoting present atoms.

the final neighbor lists, which are then accumulated into a final output. This output corresponds to a list of all sites within the minimum distance to the path.

2.5.3.3 Bias

We provide the option to perform a biased random walk by specifying the bias parameter, which consists of a direction and a strength. To achieve this, we model each step of the walk analog to a system in the canonical ensemble under the influence of an external force \mathbf{F} representing the bias. For such a system each microstate i , corresponding to the sites in the neighbor list, has the associated probability p_i given by the Gibbs–Boltzmann distribution

$$p_i = \frac{1}{Z} e^{-\beta E_i}, \quad Z = \sum_i e^{-\beta E_i},$$

where Z is the canonical partition function, $\beta = 1/k_B T$ for the boltzmann constant k_B and temperature T , and E_i the energy of site i . We model the energy of each site as the work required to move there. For a step \mathbf{s} the energy becomes $E_i = -\mathbf{s} \cdot \mathbf{F}$, where the sign is chosen such that the energy (difference) is negative when moving along the bias, analogous to an energy gain by moving there. Due to the symmetry of the random walk sites, both the atom sites and the center elements, the step length to neighboring sites will always be equal. By defining the bias strength $B = \beta |\mathbf{F}| |\mathbf{s}|$ we get that the probability for jumping to site i is

$$p_i = \frac{1}{Z} e^{B \hat{\mathbf{s}} \cdot \hat{\mathbf{F}}} \propto e^{B \hat{\mathbf{s}} \cdot \hat{\mathbf{F}}},$$

where the hat denotes the unit vector. The bias strength B then captures the opposing effects of the magnitude of the external force and the temperature of the system since $B \propto |\mathbf{F}|/T$. We notice that $\hat{\mathbf{s}} \cdot \hat{\mathbf{F}} = \cos(\theta)$ for the angle between the step and bias direction θ . This shows that the bias will have the biggest positive contribution to the probability when the step direction is fully aligned with the bias direction ($\theta = 0$), have no contribution for orthogonal directions ($\theta = \pm\pi/2$) and the biggest negative contribution when the directions are antiparallel ($\theta = \pi$). The partition function serves simply as a normalization constant. Thus, numerically we can enforce this simply by setting $Z = 1$ at first, calculating p_i , and then normalizing the result at the final stage as a division by the sum of all p_i . In the numerical implementation, we then pick the next step by the weighted discrete probability distribution p_i . In Fig. 2.13 we have illustrated how a bias of different strengths impacts the

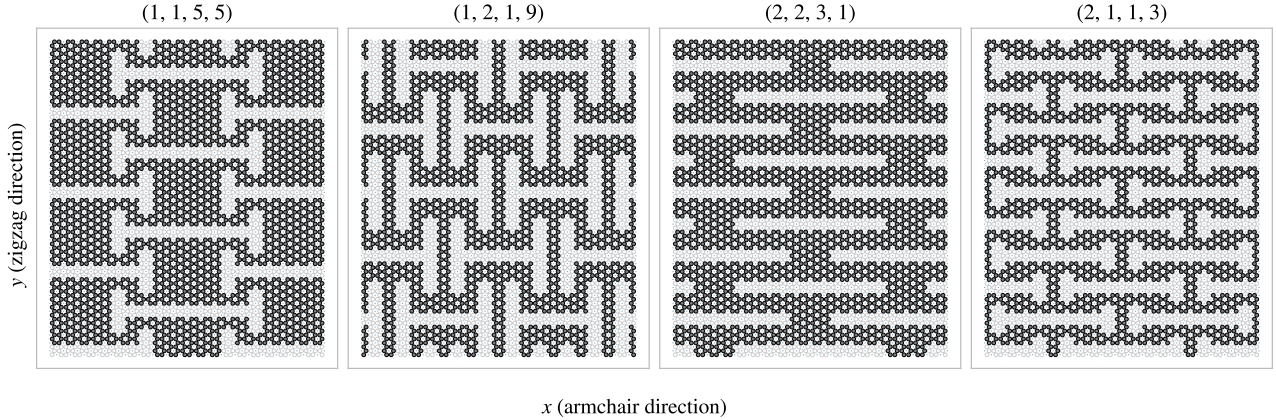


Figure 2.12: Example of different Honeycomb cut pattern variations. The specific parameters are noted as titles and all of the patterns use the center of the sheet as a reference position. The circles in the figure represent atom sites, where grey-filled circles indicate the presence of atoms and transparent circles indicate removed atoms. The blue dots in the figure indicate the center elements. The sheet matrix size is 40×80 corresponding to 3200 atom sites and an approximate sheet size of $84 \times 123 \text{ \AA}$.

probability distribution for a random walk between center elements. We can visually confirm that the bias will favor the directions that lie close to the bias direction. This preference is more distinct at high bias strengths while at low strength $B \rightarrow 0$ we get a uniform distribution that aligns with the default unbiased random walk.

2.5.3.4 Stay or break

The *stay or break* parameter defines the probability p_{stay} that the walker will keep its direction or otherwise break into a different direction by probability $1 - p_{\text{stay}}$. We implement this by altering the discrete probability used for the choice of the next step. We manually set the probability to p_{stay} for the site corresponding to a continuation in the same direction. We then normalize the distribution again. This allows us to perform a biased random walk in combination with a preference for keeping direction. For the center element walk it is trivial to determine which of the neighbor directions correspond to a continuation of direction based on the last visited site. However, for an atom site walk, it is not possible to follow the same direction in a straight line due to the hexagonal layout of the lattice. We recall that the nearest atom neighbor indexes alternate for each increment in the x or y index (see Eq. (2.3)) which corresponds to the alternating neighbor directions D as

$$(i + j) \text{ is even} \rightarrow D = \left\{ \frac{a}{2} \left(\frac{-2}{\sqrt{3}}, 0 \right), \frac{a}{2} \left(\frac{1}{\sqrt{3}}, 1 \right), \frac{a}{2} \left(\frac{1}{\sqrt{3}}, -1 \right) \right\},$$

$$(i + j) \text{ is odd} \rightarrow D = \left\{ \frac{a}{2} \left(\frac{2}{\sqrt{3}}, 0 \right), \frac{a}{2} \left(\frac{-1}{\sqrt{3}}, 1 \right), \frac{a}{2} \left(\frac{-1}{\sqrt{3}}, -1 \right) \right\}.$$

One way to mitigate this issue is to use the six directions from the center element walk as the common direction to “stay or break” from. As showcased in Fig. 2.14, in each center element direction (black arrows) there are two possible atom site directions (red and orange arrows) that are equally close to the center element direction. The red and orange arrows represent $(i + j)$ being even or odd respectively, and we notice that these appear in pairs such that we can always determine which of the atom directions is closest to the center element direction. Following this idea we can map each center direction to an atom direction depending on the even or oddness of the position. For $p_{\text{stay}} = 1$ this results in a guaranteed zigzag motion along the center element direction that it happens to start on.

The *stay or break* feature is still subject to previously defined rules. For instance, in the case where the preferred site is not available, the walker will either terminate when going there, or the preferred site is removed from the neighbor list when *avoid invalid* is set to true. In the latter case, the walker will be forced to break out of its direction and follow the new direction that it happens to choose.

Table 2.3: Parameters for the random walk generator.

Parameters	Value	Description
Num. walkers (M)	Integer ≥ 1	Number of random walks to be initiated on the sheet (one at a time).
Max. steps (S)	Integer ≥ 1	The maximum steps allowed for any random walker.
Min. distance	Integer ≥ 0	The minimum distance required between any future paths and the previous paths in terms of the shortest walking distance in between.
Bias	(direction, strength ≥ 0)	Bias direction and strength defining the discrete probability for the choice of the next site.
Connection	Atoms / Center elements	Whether to walk between atom sites or center elements removing all adjacent atoms.
Avoid invalid	True/False	Whether to remove already visited sites from the neighbor list before picking the next site. This prevents jumping to already visited sites and lowers the likelihood of early termination.
Stay or break	$p = [0, 1]$	Probability that the walker will maintain its direction for the next step.
Periodic	True/False	Whether to use periodic boundary conditions on all four sides.
Avoid clustering	Integer ≥ 0	Amount of times to restart the whole random walk generation in order to arrive at a non-detached configuration. If no valid configuration is reached after this amount of tries, the non-spanning clusters are removed.
RN6	True/False	Randomly change the bias direction between the deployment of each random walker to one of the six center element directions.
Grid start	True/False	The option to have the random walkers start in an evenly spaced grid.
Centering	True/False	Relocate the path of a random walk after termination such that the path center of mass gets closer to the starting point (without violating the rules regarding already visited sites).

2.5.3.5 Deployment schemes

By default, each random walker is given a uniform random starting point among the non-visited available sites left on the sheet. This includes any modifications in relation to the minimum distance parameter. By setting the *grid start* parameter to true, the starting points are instead predefined on an evenly spaced grid. That is, the sheet is subdivided into the least amount of squares that will accommodate space for each starting point. 1 walker leads to a 1×1 partition, $\{2, 3, 4\}$ walkers lead to a 2×2 partition, $\{5, 6, 7, 8, 9\}$ walker lead to a 3×3 partition and so on. For each partition square, the starting point is placed as centrally as possible. The lower left partition square is then chosen as a default starting place for the first walker and the remaining sites are filled according to the order that maximizes the minimum distance between a new starting point and the ones already used³. An example of the deployment is shown in Fig. 2.15.

The *centering* parameter lets us relocate the path of the random walker such that the path center of mass gets closer to the starting point. When toggled on, the path is moved in the direction defined by the center of mass and the starting point for which the closest valid relocation on the direct translation line is chosen. This can be used in combination with the *grid start* and the *bias parameter* to make rather ordered configurations. In

³In hindsight, it would have been less biased to choose a random partition square as the starting one, but we do not consider this to be of great importance for the usage of this feature in final dataset

Algorithm 1 Recursive algorithm implemented as a class method of the random walk generator. For a given path input it flags all sites within a distance given by the class attribute `self.min_dis`.

```

Require: self.min_dis > 0
1: function WALK_DISTANCE(self, input, dis = 0, pre = [ ])
2:   new_neigh ← [ ]                                     ▷ Initialize list for new neighbors
3:   for site in input do
4:     neigh ← get_neighboring_sites(site)                ▷ Get surrounding neighbors
5:     for n in neigh do
6:       if (n not in pre) and (n not in new_neigh) then      ▷ If not already added
7:         AddItem(new_neigh, n)                            ▷ then add the site
8:       end if
9:     end for
10:    end for                                         ▷ Increment distance counter
11:    dis += 1                                         ▷ Max limit hit
12:    if dis ≥ self.min_dis then
13:      return input + new_neigh
14:    else                                              ▷ Start a new walk from each of the neighboring sites
15:      pre ← input
16:      return pre + self.walk_distance(new_neigh, dis, pre)
17:    end if
18: end function

```

addition, the *RN6* parameter can be used to update the bias direction to one of the six center element directions for each new walker deployed. This lets us create configurations like the one shown in Fig. 2.16b.

2.5.3.6 Validity

The simulation procedure requires the sheet to be fully attached, non ruptured, which can be summarized as the following requirements.

1. There exist only a single cluster on the sheet. We define a cluster as the set of atoms which can all be reached through nearest neighbour walking on the cluster.
2. The cluster of atoms is spanning the sheet in the y-direction. This means that there exist at least one path through nearest neighbour walks that connect the bottom and the top of the sheet. This is due to the reason that the sheet must be attached to the pull blocks.

In order to accommodate these requirements we count the number of clusters and search for a spanning cluster after all walkers have terminated. If the requirements are not met we simply rerun the random walk from scratch. This is done according to *avoid clustering* parameter which takes integer values corresponding to the number of times to repeat this process. If the requirements are not met during any of those reruns the non-spanning clusters are simply removed. In the case of no spanning cluster the configuration is skipped. This crude scheme was later reinvented as a more refined repair scheme which alters the sheet by the intention of performing the least amount of changes (addition or subtraction of atoms) in order to meet the attachment requirements. This was done as a part of the accelerated search procedure and hence it was not utilized in the creation of the random walk dataset.

Talk about the new repair algorithm

2.5.3.7 Random walk examples

Some examples of the random walk patterns are illustrated in Fig. 2.16.

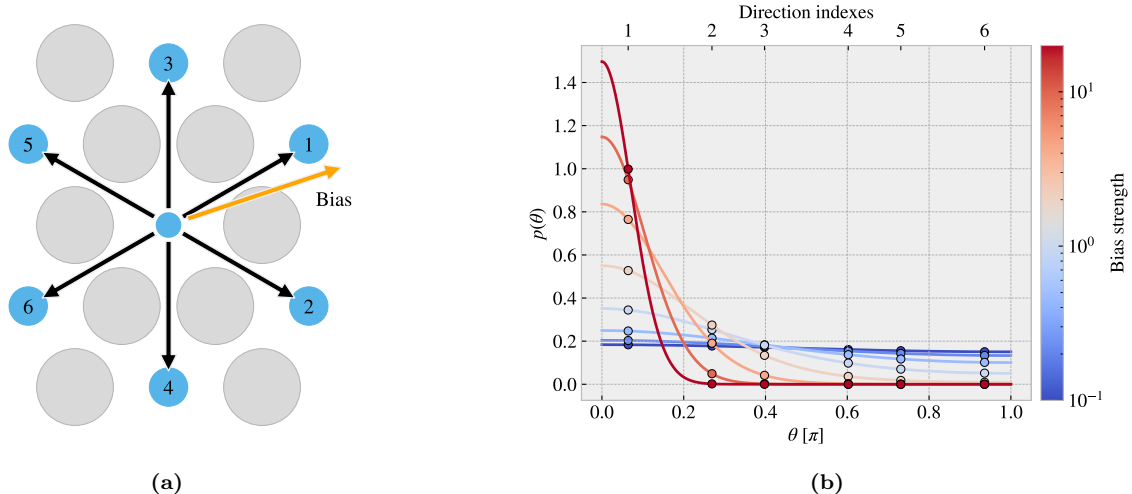


Figure 2.13: Illustration of the probability distribution for the various step directions during a biased random walk between center elements. (a) The possible step directions are represented by black arrows that point towards the neighboring center elements depicted as blue circles. The bias direction is denoted by an orange arrow, and the numbering indicates the most probable direction (1) towards the least probable direction (6). The atom sites are marked as grey circles for reference. (b) The probability distribution as a function of the angle θ between the step direction and the bias direction. The distribution is normalized according to the discrete probabilities marked with dots for which the continuous line simply highlights the shape of the distribution. The direction indexes correspond to the numbering on panel (a). The color map indicates different strengths of the bias.

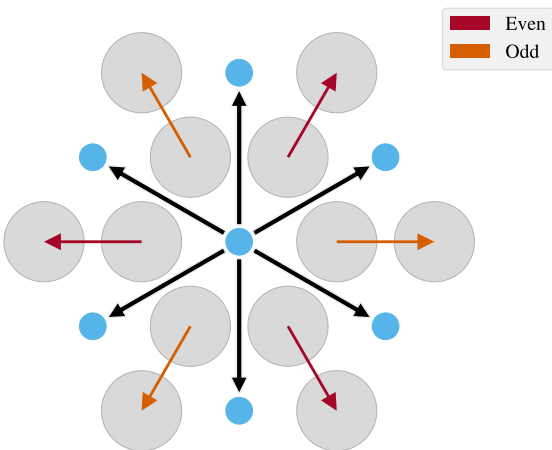


Figure 2.14: Visualization of the center element directions (black arrows) connecting the center elements depicted as blue dots, and the atom site directions (red and orange arrows) connection the atom sites depicted as grey circles. The red arrows correspond to the case where the sum of the atom site indexes (i, j) is even, while the orange arrows correspond to the case where the sum is odd. Notably, for each case, there is always one atom site direction that is uniquely closest to a given center element direction.

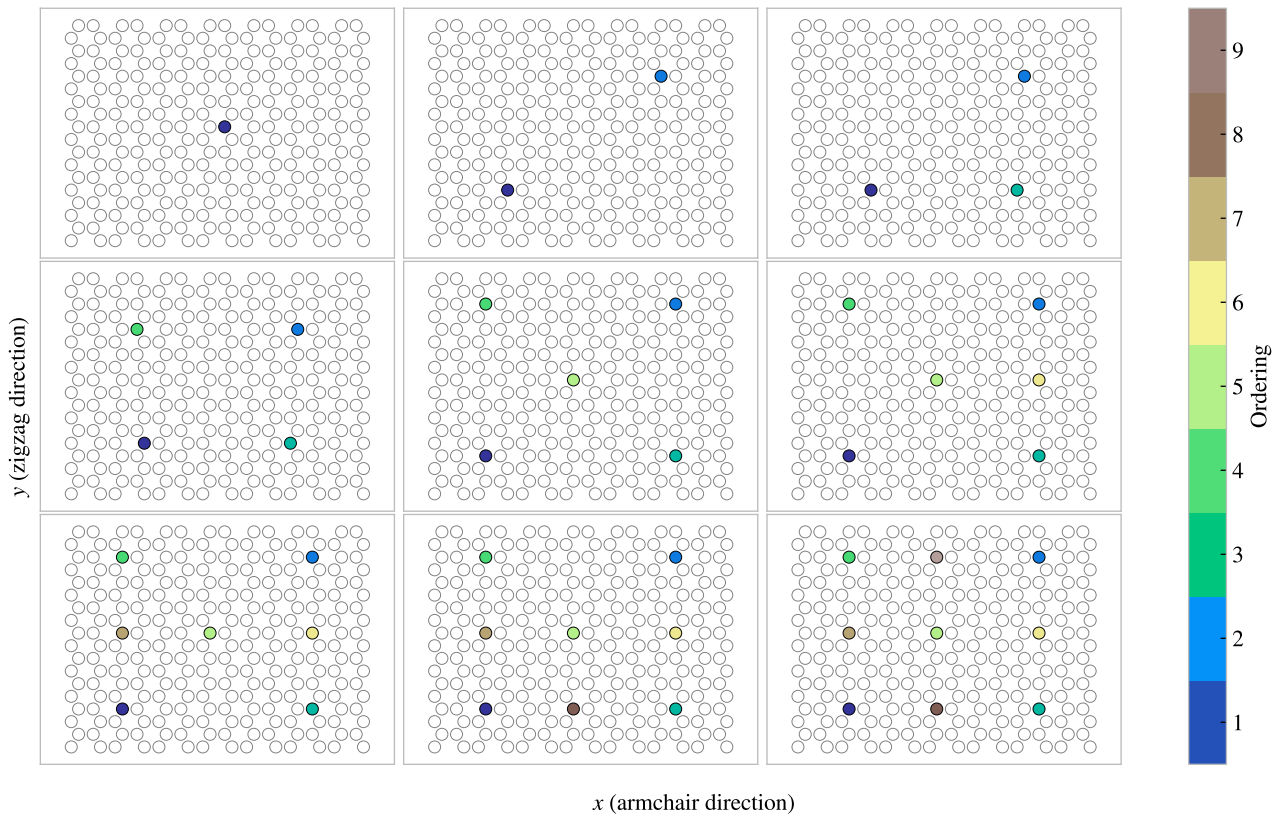


Figure 2.15: The figure illustrates the distribution of starting points when the *grid start* parameter is turned on for a 14×18 sheet, for varying numbers of deployed random walkers ranging from 1 to 9. The color map is used to indicate the order in which the walkers were deployed.

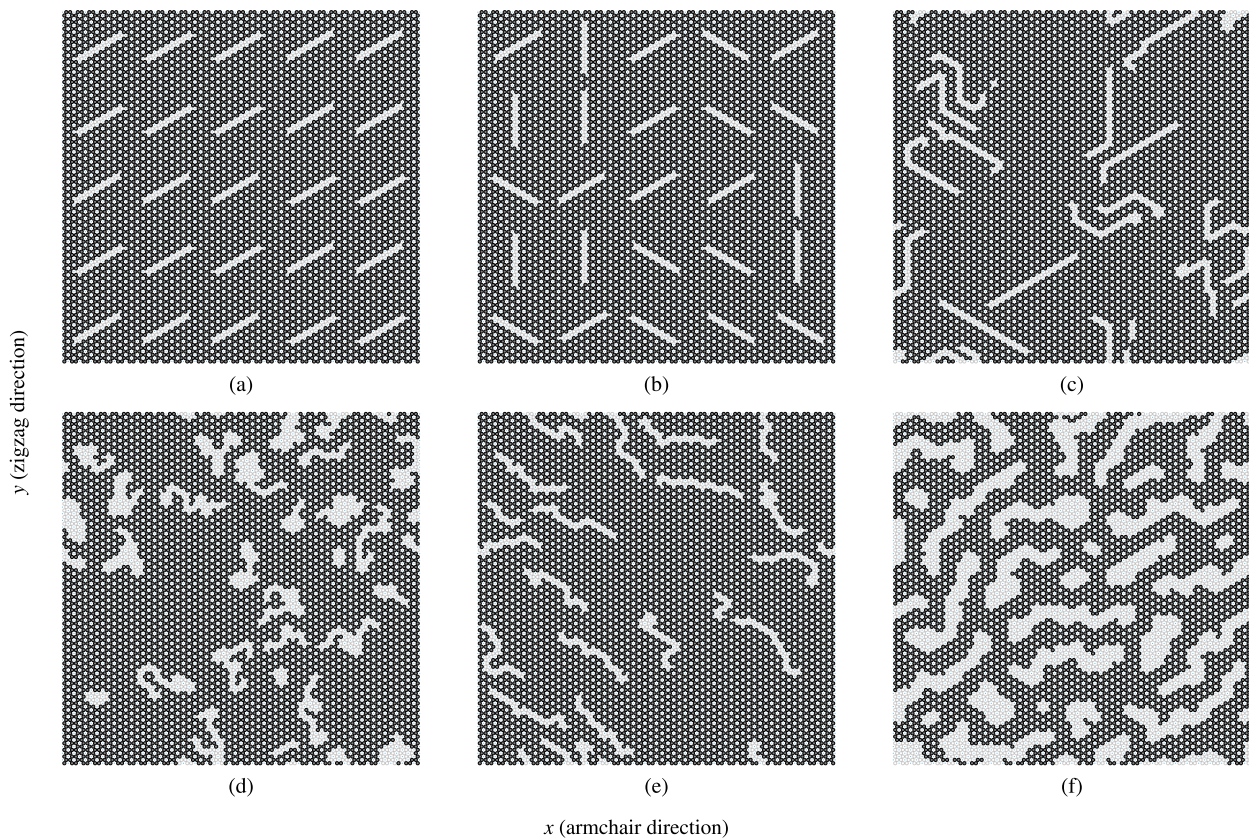


Figure 2.16: Some example uses of the random walking class. Give information of parameters? Henrik says Yes :D

Chapter 3

Summary

In this thesis, we have studied the nanoscale friction of a Kirigami graphene sheet under the influence of load and strain using MD simulations. We have developed a numerical framework for generating diverse Kirigami designs which we have utilized to create a dataset for the frictional behavior depending on Kirigami pattern, strain, and loading. Our findings suggest that the frictional behavior of a Kirigami sheet is highly dependent on the geometry of the pattern and the strain conditions. We observed that the out-of-plane buckling can be associated with a non-linear friction-strain curve which can be utilized to demonstrate a negative friction coefficient in a system with coupled load and strain. Moreover, we have investigated the possibility to use machine learning on this dataset and attempted an accelerated search. Our findings imply that machine learning can be feasible for this approach, additional data is required to establish a more reliable foundation for a search for new Kirigami patterns. In this chapter, we will provide a summary of our findings and draw conclusions based on the results obtained. Finally, we will suggest some topics for further research.

3.1 Summary and conclusions

3.1.1 Designing an MD simulation

We have designed an MD simulation for the examination of friction for a graphene sheet sliding on a silicon substrate. The key system features were the introduction of the pull blocks, defined as the end regions of the sheet with respect to the sliding direction, which was utilized for applying normal load and sliding the sheet. The pull blocks were made partly rigid and used to employ a thermostat as well. Through an analysis of the friction forces retrieved from sliding simulations, we have established a standardized metric for kinetic friction. In particular, we measured the force exerted by the substrate on the full sheet, including the pull blocks, with respect to the sliding direction, and determined the kinetic friction as the mean value of the last half of the simulation. The uncertainties were estimated based on the fluctuations in the running mean. We found that the assessment of static friction was ambiguous for our simulation and did not pursue this further. From the analysis of the force traces, friction force vs. time, we identify the friction behavior in our simulation domain as being in the smooth sliding regime. This is attributed to the choice of a relatively high sliding speed (20 m/s) and infinitely stiff springs for the tethering of the sheet. This was supported by a demonstration of a transition to the stick-slip regime through the use of softer springs and a decrease in sliding speed. By conducting a more systematic investigation of the effects of temperature, sliding speed, spring constant and timestep, we identified a set of default values based on numerical stability and computational cost. During this process, we aimed to select the variables that would maintain a relatively stable measured friction with moderate perturbations around these default values. We found that friction increased with temperature which we attribute to being in the ballistic sliding regime. In the absence of clear indications from the investigation regarding an appropriate temperature, we opted for the standard choice of room temperature, 300 K. Furthermore, we found friction to increase with velocity as expected, with some signs of phonon resonance at certain sliding speeds as well. We chose a rather high velocity of 20 m/s mainly for the consideration of computational costs. For the spring constant, we found decreasing friction with increasing stiffness of the springs. This is associated with the transition from a stick-slip-influenced regime toward smooth sliding and can be attributed to an underlying change in commensurability. The choice of an infinitely stiff spring was made from an assessment of the variation

in friction with perturbations in the spring constant value. Finally, we confirmed that a timestep of 1 fs provides reasonable numerical stability. However, based on fluctuations with timestep we find that the uncertainty in the simulations might be higher than first estimated. For the non-strained Kirigami sheet, these fluctuations were on the order of ± 0.017 nN for the evaluation of the kinetic friction.

3.1.2 Generetig Kirigami patterns

In order to investigate the effects of Kirigami design we have created a numerical framework for generating various patterns. By defining an indexing system for the hexagonal lattice structure we were able to define the Kirigami designs as a 2D binary matrix for numerical implementation. We have selected two macroscale designs, which we denote the *Tetrahedron* and *Honeycomb* patterns, based on their ability to exhibit out-of-plane buckling when subjected to strain. By digitalizing the designs to match the hexagonal graphene lattice, we found that the characteristic design features can be translated to the nanoscale, as we observed similar out-of-plane buckling in MD simulations. Through our numerical framework we were able to create an ensemble of perturbed unique variations which yielded approximately 135×10^3 and 2.025×10^6 unique configurations for the Tetrahedron and Honeycomb patterns respectively. When considering the possibility to translate the periodic patterns on the graphene sheet the number of possible patterns can be increased by approximately a factor of 100. To introduce some random design features, we have developed a framework for generating Kirigami patterns based on random walks. The framework includes mechanisms such as bias, avoidance of existing cuts, preference for maintaining a direction, and procedures for repairing the sheet for simulation purposes. In general, we found that the capabilities of this numerical framework for generating Kirigami designs exceeded our computational resources with regard to performing MD simulation under different loads and strains for each of the designs. In general, we found that the computational capacity of our numerical framework for generating Kirigami designs surpassed our available resources for conducting MD simulations under various load and strain for each design. Our MD-based dataset only utilized a subset of configurations with 9660 data points based on 216 Kirigami configurations (Tetrahedron: 68, Honeycomb: 45, Random walk: 100, Pilot study: 3). Hence, we argue that the Kirigami generative framework can be valuable for further studies on an extended dataset.

3.1.3 Control friction using Kirigami

We have investigated the frictional behavior of the Tetrahedron and Honeycomb patterns in comparison to a non-cut sheet under various strains and loads. Initially, we observed that straining the Kirigami sheets in a vacuum resulted in an out-of-plane buckling. When adding the substrate to the simulation this translated into a decreasing contact area with strain. We found the Honeycomb sheet to exhibit the most significant buckling with a corresponding reduction of relative contact area to approximately 43%, whereas the non-cut sheet did not produce any significant buckling in comparison. For the Kirigami sheets, we found that friction initially increased with strain, which made for increasing friction with decreasing contact area. As the strain continued to increase the friction-strain curve exhibited highly non-linear trends with strong negative slopes as well (see ??). During the full strain, the contact area was decreasing monotonically except for a slight increase just before rupturing. These results contradict the asperity theory hypothesis of decreasing friction with decreasing contact area, and we conclude that no clear relationship between friction and contact area can be made. The non-cut sheet did not show any significant dependency on the strain as both the friction and the contact area remained constant with strain. Thus our findings suggest that a changing contact area and the strain-induced friction effects might be associated through an underlying mechanism connected to the buckling of the sheet. We did find some independent effects from the introduciton of Kirigami cuts before applying strain. We observed a small increase in friction between the non-cut sheet and the Kirigami sheet, but this was one order of magnitude lower than the effects associated with the strain in combination. Since the strained non-cut sheet did not exhibit any significant effects from strain we conclude that the independent effects from Kirigami cuts and tension in the sheet cannot be regarded as a dominating mechanism for friction. When considering the friction dependency with load, we generally found a weak dependency corresponding to a friction coefficient on the order of 10^{-4} – 10^{-5} even though we could not confirm any clear relationship. This is best attributed to a superlubric state of the graphene sheet as seen in other studies as well. The slope of the friction-load curve was not considerably affected by the straining of the Kirigami sheet which led us to the conclusion that strain-induced effects are dominant in comparison to any load-related effects. In summary, we have found clear evidence that the friction in the Kirigami sheet system is controlled by strain.

When considering our findings in light of previous related results we find it plausible that the governing mechanism for the observed friction effects is related to commensurability. Since we have observed extremely low friction in our system, we argue that the non-deformed sheet corresponds to an incommensurable configuration. This is supported by the fact that we were not able to lower the friction from the original starting point. Additionally, this also aligns with the observation that the introduction of the non-strained Kirigami designs increased friction slightly. Since some atoms were removed from the lattice this can be hypothesized to relax the incommensurability to some degree. When the Kirigami sheet buckles during stretching, it allows for a considerable rearrangement of the atoms in contact with the substrate. Hence, it may transition in and out of commensurable configurations, which could explain the non-linear trend for the friction-strain curve. One way to test this hypothesis is to reorientate the sheet in order to reach a commensurable start configuration. Then we might find a transition from a commensurable to an incommensurable case during the initial straining which would result in a lowering in friction with respect to the starting point.

3.1.4 Capturing trends in friction data with machine learning

By utilizing the numerical framework for generating Kirigami design we have created a MD-based dataset for the frictional behavior depending on Kirigami designs, load and strain. The dataset reveals some general correlations with mean friction, such as a positive correlation to strain (0.77) and porosity (0.60), and a negative correlation to contact area (-0.67). These results align with the finding in the pilot study, suggesting that the change in friction is associated with cuts in the sheet (porosity) and a changing contact area.

By defining the friction property metrics: $\min F_{\text{fric}}$, $\max F_{\text{fric}}$, $\max \Delta F_{\text{fric}}$ and $\max \text{drop}$ (maximum decrease in friction with strain), we investigated the top design candidates within our dataset. From these results, we found no indication for the possibility to reduce friction with the Kirigami approach since the non-cut sheet provided the lowest overall friction. Furthermore, among the top candidates, we found that a flat friction-strain profile is mainly associated with little decrease in the contact area and vice versa. These observations are consistent with the results of the pilot study and support the hypothesis that commensurability plays a key role in governing the behavior of the system. In terms of the maximum properties, we observed an improvement compared to the values obtained in the pilot study, with the Honeycomb pattern exhibiting the highest scores. This indicates that the data may be useful for optimizing these properties.

For the machine learning investigation, we have implemented a VGGNet-16-inspired convolutional neural network with a deep “stairlike” architecture: C32-C64-C128-C256-C512-C1024-D1024-D512-D256-D128-D64-D32, for convolutional layers C with the number denoting channels and fully connected (dense) layers D with the number denoting nodes. The final model contains 1.3×10^7 parameters and was trained using the ADAM optimizer for a cyclic learning rate and momentum scheme. We trained the network for a total 1000 epochs while saving the best model during training based on the validation score. The model validation performance gives a mean friction R^2 score of $\sim 98\%$ and a rupture accuracy of $\sim 96\%$. However, we got lower scores for a selected subset of the Tetrahedon ($R^2 \sim 88.7\%$) and Honeycomb ($R^2 \sim 96.6\%$) pattern based on the top 10 max drop scores respectively. The scores obtained were lower, even though the selected configurations were partly included in the training data and the hyperparameter selection favored the performance on this selected set. Thus we conclude that these selected configurations, associated with a highly non-linear friction-strain curve, represent a bigger challenge for the machine learning prediction. One interpretation is that these involve the most complex dynamics and perhaps that this is not readily distinguished from the behavior of the other configurations which constitute the majority of the data set. By evaluating the ability of the model to rank the dataset based on property scores, we found that it was able to effectively represent the top three scores for the maximum categories. However, the ranking for the minimum friction property was lacking. We attribute this discrepancy to the fact that this property requires a higher level of precision, which the model was not able to achieve. To obtain a more accurate evaluation of the model’s performance, we generated a test set using MD simulations for the random walk based suggestions obtained from the accelerated search. The results showed a significantly worse performance compared to the validation set, with a two-order of magnitude higher loss and a negative R^2 score for the mean friction property. The negative R^2 score suggests that the model’s predictions were worse than simply predicting the mean value of the true data.

However, by reevaluating the hypertuning and choosing solely on the basis of validation loss, we still found poor results on the test set. This suggests that the inadequate performance is not solely due to biased hypertuning but rather because our original dataset did not sufficiently cover a diverse range of Kirigami configurations to accurately capture the full complexity of its frictional behavior. The validation scores indicate that the use of

machine learning is a feasible approach for addressing this problem, as we were able to identify some general trends in the data. Nonetheless, from the test scores, it is evident that further improvements to the dataset are necessary in order to develop a reliable model.

3.1.5 Accelerated search

Using the ML model we performed two types of accelerated search. One by evaluating the property scores of an extended dataset and another with the use of the genetic algorithm approach. For the extended dataset search, we used the developed pattern generators to generate 1.35×10^6 Tetrahedron, 2.025×10^7 Honeycomb and 10 k Random walk patterns. The search results for the minimum friction property indicate a preference for low cut density or low porosity. This aligns with the overall observation that the dataset does not provide any suggestions to further reduction in friction, as the non-cut sheet has the lowest friction.

The search for the maximum properties resulted in some minor score increases but the suggested candidates were mainly overlapping with the original dataset. By investigating the sensitivity to translations of the Tetrahedron and Honeycomb patterns, we observed significant variations in the model's predictions with only minor translations. This can be attributed to a physical dependency since these translations affect the edge of the sheet. However, given the poor model performance on the test set, we believe it is more likely that this variation is due to an insufficiency in the model caused by the limitations of the dataset.

In our investigation of the genetic algorithm approach, we used a starting population that was based on the results from the extended dataset accelerated search, as well as some randomly generated initializations with different porosity values. However, this approach did not provide any noteworthy indication for new design structures worth more investigation. In general, the initialization of the population itself proved to be a more promising strategy than the genetic algorithm. We acknowledge that further effort could potentially yield useful results with the genetic algorithm approach. However, we believe that the current lack of promising results can be attributed to the uncertainty of the model which where the reason for not pursuing this any further.

By considering the Grad-CAM explanation method, we observed that the model predictions were often substantially reliant on the top and bottom edges of the Kirigami configurations. This was unexpected since these edges are not true edges but are connected to the pull blocks used in the simulation. Despite the model's uncertain predictions, we speculate that this may be due to the thermostat effects from the pull blocks. Therefore, we note this as a feature worth investigating in the simulations.

3.1.6 Negative friction coefficient

Based on our initial investigations of the Kirigami sheet, we have discovered a highly non-linear friction-strain relationship. By proposing a linear coupling between load and strain with ratio R , we find that these results suggest the possibility to utilize the negative slope on the friction-strain curve to achieve a negative friction coefficient. Based on the drop from top to bottom of these curves, using the Tetrahedron (7, 5, 1) and Honeycomb (2, 2, 1, 5) pattern from the pilot study, we estimate that the average coefficient within this range will be $-R12.75$ nN for the Tetrahedron pattern and $-R \cdot 2.72$ nN for the Honeycomb pattern.

To investigate this hypothesis, we conducted a simulation with a coupling between load and sheet tension, mimicking a nanomachine attached to the sheet, using the Kirigami configurations from the Pilot study. We observed that the non-linear behavior in the friction-strain curve also translated into a non-linear friction-load relationship for the coupled system. Additionally, we found that the Honeycomb pattern exhibited a non-linear strain-tension curve which resulted in an almost discontinuous increase in friction for the initial increase in load. We attribute this feature to an unfolding process visually confirmed from the simulation frames. For the coupled system with a load-to-tension ratio of 6 we found regions in the friction-load curve with significant negative slopes. By considering the maximum and minimum points for such regions we estimated the average friction coefficient to be -0.31 in the load range $F_N = [4.65, 6.55]$ nN for the Tetrahedron pattern and -0.38 in the range $F_N = [0.71, 4.31]$ nN for the Honeycomb pattern. These results can be scaled by adjusting the load-to-tension ratio.

Based on our investigations, we have found that the combination of Kirigami cuts and strain has significant potential for controlling friction. Specifically, we have demonstrated that by enforcing a coupling between load and strain through tension, it is possible to achieve a negative friction coefficient. Therefore, we believe that this approach could be promising for developing novel friction-control strategies.

3.2 Outlook

In this thesis, we have demonstrated that certain Kirigami designs exhibit non-linear friction behavior with strain. This discovery was made through an exploration of different designs, which invites further investigation into the underlying mechanisms of this phenomenon. To this end, it would be valuable to one or two selected designs, such as the Tetrahedron and Honeycomb patterns, and study the effects of various physical parameters on the friction-strain curve.

First of all, we suggest an investigation of how the friction-strain curve depends on temperature, sliding speed, spring constant, and loads for an increased range $F_N > 100nN$. This is especially interesting in the context of physical conditions leading to a stick-slip behavior since our study takes a basis in smooth sliding friction. Moreover, it would be valuable to verify that the choices for relaxation time, pauses, interatomic potentials and substrate material are not critical for the qualitative observations. Especially the Adaptive Intermolecular Reactive Empirical Bond Order (AIREBO) potential for the modeling of the graphene sheet might be of interest. In this context, it might also be useful to investigate the effects of excluding adhesion from the simulations.

In order to investigate the hypothesis of commensurability as a governing mechanism we suggest an investigation of the friction-strain curve for different scan angles. If commensurability is an important factor, we hypothesize that the friction-strain curve will exhibit different qualitative shapes at varying scan angles. Additionally, it may be interesting to investigate the friction-strain relationship under a uniform load to gain insight into how the loading distribution affects the out-of-plane buckling and associated commensurability effect.

Another topic worth studying is the relation to scale and edge effects. This includes an investigation of scaling effects, considering the ratio of the sheet area to the edge length, but also a translation of the sheet patterns to study the presence of any Kirigami-induced edge effects. The latter is motivated by the findings from the machine learning predictions. With this regard, we would also suggest a more detailed study of the effect of the thermostat in the pull blocks which is suggested to have a possible importance when judging from the Grad-CAM analysis.

Regarding the machine learning approach, our findings indicate that there is a significant need to expand the dataset. In order to get more insight into this issue one could use unsupervised clustering techniques like the t-Distributed Stochastic Neighbor Embedding (t-SNE) to visualize the distribution of Kirigami configurations in the dataset. Another valuable approach is the active learning method similar to that used by Hanakata et al. [6]. That is, we extend the dataset using the top candidates of a machine learning-driven accelerated search and repeat the process of training the model, searching for new candidates and extending the dataset. This provides a direction for the extension of the dataset which could lead to a more efficient approach to address the complex space of Kirigami designs. We note that one can also create a dataset of a fixed kirigami designs and vary the physical parameters to support the investigations mentioned above. For both variations we believe that the results could benefit from a consideration of more advanced model architectures and machine learning techniques. If successful this would invite further studies of inverse design methods such as GAN or diffusion models.

Appendices

Appendix A

Appendix A

Appendix A

Appendix B

Appendix B

Appendix C

Bibliography

- ¹E. Gnecco and E. Meyer, *Elements of friction theory and nanotribology* (Cambridge University Press, 2015).
- ²Bhusnur, “Introduction”, in *Introduction to tribology* (John Wiley & Sons, Ltd, 2013) Chap. 1, 1–?
- ³H.-J. Kim and D.-E. Kim, “Nano-scale friction: a review”, *International Journal of Precision Engineering and Manufacturing* **10**, 141–151 (2009).
- ⁴K. Holmberg and A. Erdemir, “Influence of tribology on global energy consumption, costs and emissions”, *Friction* **5**, 263–284 (2017).
- ⁵B. Bhushan, “Gecko feet: natural hairy attachment systems for smart adhesion – mechanism, modeling and development of bio-inspired materials”, in *Nanotribology and nanomechanics: an introduction* (Springer Berlin Heidelberg, Berlin, Heidelberg, 2008), pp. 1073–1134.
- ⁶P. Z. Hanakata, E. D. Cubuk, D. K. Campbell, and H. S. Park, “Accelerated search and design of stretchable graphene kirigami using machine learning”, *Phys. Rev. Lett.* **121**, 255304 (2018).
- ⁷P. Z. Hanakata, E. D. Cubuk, D. K. Campbell, and H. S. Park, “Forward and inverse design of kirigami via supervised autoencoder”, *Phys. Rev. Res.* **2**, 042006 (2020).
- ⁸L.-K. Wan, Y.-X. Xue, J.-W. Jiang, and H. S. Park, “Machine learning accelerated search of the strongest graphene/h-bn interface with designed fracture properties”, *Journal of Applied Physics* **133**, 024302 (2023).
- ⁹Y. Mao, Q. He, and X. Zhao, “Designing complex architectured materials with generative adversarial networks”, *Science Advances* **6**, eaaz4169 (2020).
- ¹⁰Z. Yang, C.-H. Yu, and M. J. Buehler, “Deep learning model to predict complex stress and strain fields in hierarchical composites”, *Science Advances* **7**, eabd7416 (2021).
- ¹¹A. E. Forte, P. Z. Hanakata, L. Jin, E. Zari, A. Zareei, M. C. Fernandes, L. Sumner, J. Alvarez, and K. Bertoldi, “Inverse design of inflatable soft membranes through machine learning”, *Advanced Functional Materials* **32**, 2111610 (2022).
- ¹²S. Chen, J. Chen, X. Zhang, Z.-Y. Li, and J. Li, “Kirigami/origami: unfolding the new regime of advanced 3D microfabrication/nanofabrication with “folding””, *Light: Science & Applications* **9**, 75 (2020).
- ¹³OpenAI, *Dall-e2*, 2023.
- ¹⁴Midjourney, *Midjourney*, 2023.
- ¹⁵Z. Deng, A. Smolyanitsky, Q. Li, X.-Q. Feng, and R. J. Cannara, “Adhesion-dependent negative friction coefficient on chemically modified graphite at the nanoscale”, *Nature Materials* **11**, 1032–1037 (2012).
- ¹⁶B. Liu, J. Wang, S. Zhao, C. Qu, Y. Liu, L. Ma, Z. Zhang, K. Liu, Q. Zheng, and M. Ma, “Negative friction coefficient in microscale graphite/mica layered heterojunctions”, *Science Advances* **6**, eaaz6787 (2020).
- ¹⁷D. Mandelli, W. Ouyang, O. Hod, and M. Urbakh, “Negative friction coefficients in superlubric graphite–hexagonal boron nitride heterojunctions”, *Phys. Rev. Lett.* **122**, 076102 (2019).
- ¹⁸R. W. Liefferink, B. Weber, C. Coulais, and D. Bonn, “Geometric control of sliding friction”, *Extreme Mechanics Letters* **49**, 101475 (2021).
- ¹⁹M. Metzsch, *Tuning Frictional Properties of Kirigami Altered Graphene Sheets using Molecular Dynamics and Machine Learning*.

- ²⁰A. P. Thompson, H. M. Aktulga, R. Berger, D. S. Bolintineanu, W. M. Brown, P. S. Crozier, P. J. in 't Veld, A. Kohlmeyer, S. G. Moore, T. D. Nguyen, R. Shan, M. J. Stevens, J. Tranchida, C. Trott, and S. J. Plimpton, “LAMMPS - a flexible simulation tool for particle-based materials modeling at the atomic, meso, and continuum scales”, *Comp. Phys. Comm.* **271**, 108171 (2022).
- ²¹E. M. Nordhagen, *LAMMPS simulator*.
- ²²A. H. Larsen, J. J. Mortensen, J. Blomqvist, I. E. Castelli, R. Christensen, M. Dułak, J. Friis, M. N. Groves, B. Hammer, C. Hargus, E. D. Hermes, P. C. Jennings, P. B. Jensen, J. Kermode, J. R. Kitchin, E. L. Kolsbjergr, J. Kubal, K. Kaasbjerg, S. Lysgaard, J. B. Maronsson, T. Maxson, T. Olsen, L. Pastewka, A. Peterson, C. Rostgaard, J. Schiøtz, O. Schütt, M. Strange, K. S. Thygesen, T. Vegge, L. Vilhelmsen, M. Walter, Z. Zeng, and K. W. Jacobsen, “The atomic simulation environment—a python library for working with atoms”, *Journal of Physics: Condensed Matter* **29**, 273002 (2017).
- ²³A. Paszke, S. Gross, F. Massa, A. Lerer, J. Bradbury, G. Chanan, T. Killeen, Z. Lin, N. Gimelshein, L. Antiga, A. Desmaison, A. Kopf, E. Yang, Z. DeVito, M. Raison, A. Tejani, S. Chilamkurthy, B. Steiner, L. Fang, J. Bai, and S. Chintala, “Pytorch: an imperative style, high-performance deep learning library”, in *Advances in neural information processing systems* **32** (Curran Associates, Inc., 2019), pp. 8024–8035.
- ²⁴D. Gray, A. McCaughan, and B. Mookerji, “Crystal structure of graphite, graphene and silicon”, *Physics for Solid State Applications* **6**, 730 (2009).
- ²⁵L. Burrows, *New pop-up strategy inspired by cuts, not folds*, (Feb. 24, 2017) <https://seas.harvard.edu/news/2017/02/new-pop-strategy-inspired-cuts-not-folds>.
- ²⁶*Scotch cushion lock protective wrap*, https://www.scotchbrand.com/3M/en_US/scotch-brand/products/catalog/~/Scotch-Cushion-Lock-Protective-Wrap/?N=4335+3288092498+3294529207&rtr=rud.